Neuron

Article

Delayed maturation and migration of excitatory neurons in the juvenile mouse paralaminar amygdala

Graphical abstract

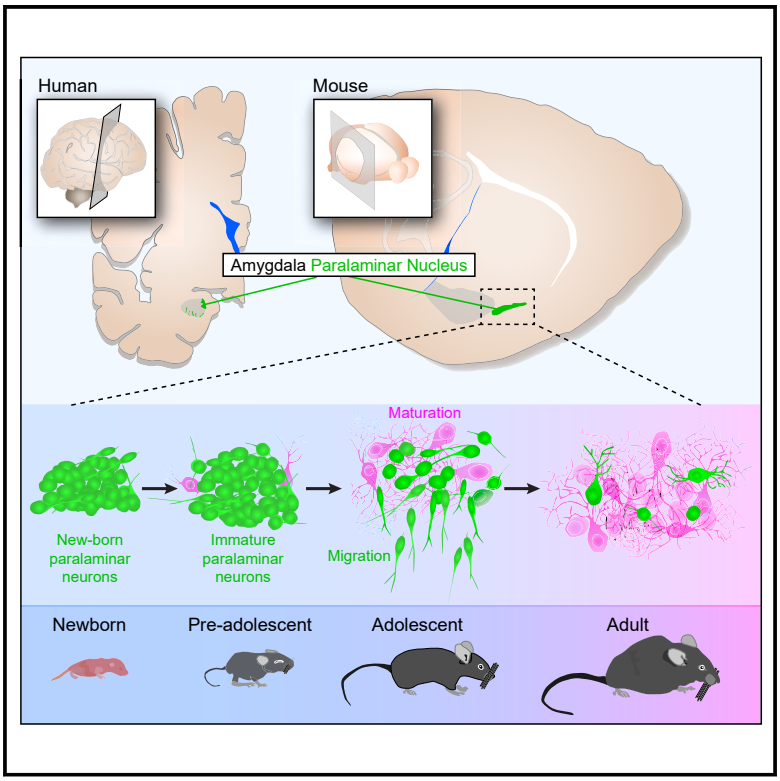

Authors

Pia J. Alderman, David Saxon, Lucía I. Torrijos-Saiz, ..., Vicente Herranz-Pérez, Joshua G. Corbin, Shawn F. Sorrells

Correspondence

shawn.sorrells@pitt.edu

In brief

Similar to humans, mice have a paralaminar amygdala region containing immature excitatory neurons. These neurons are not produced by ongoing neurogenesis but are born embryonically and delay their maturation. In juvenile-adolescent ages, some migrate into the nearby cortex, and others begin to mature locally, developing selective responses to olfactory stimuli.

Highlights

- Like humans, mice have a paralaminar amygdala with immature excitatory neurons
- PL neurons are born embryonically, and most delay maturation until early adolescence
- Some PL neurons migrate into the ventral endopiriform cortex during early adolescence
- Immature PL neurons develop responses to olfactory stimuli prior to adulthood

Alderman et al., 2024, Neuron *112*, 1–19
February 21, 2024
https://doi.org/10.1016/j.neuron.2023.11.010

CellPress

Please cite this article in press as: Alderman et al., Delayed maturation and migration of excitatory neurons in the juvenile mouse paralaminar amygdala, Neuron (2023), https://doi.org/10.1016/j.neuron.2023.11.010

Neuron

CellPress

Article

Delayed maturation and migration of excitatory neurons in the juvenile mouse paralaminar amygdala

Pia J. Alderman,[1] David Saxon,[2,3] Lucía I. Torrijos-Saiz,[4] Malaz Sharief,[1] Chloe E. Page,[1] Jude K. Baroudi,[1] Sean W. Biagiotti,[1] Vladimir A. Butyrkin,[2,5] Anna Melamed,[1] Chay T. Kuo,[6] Stefano Vicini,[3,7] Jose M. García-Verdugo,[4,8] Vicente Herranz-Pérez,[4,8] Joshua G. Corbin,[2] and Shawn F. Sorrells[1,9,10,*]

[1]Department of Neuroscience, University of Pittsburgh, Pittsburgh, PA 15260, USA
[2]Center for Neuroscience Research, Children's Research Institute, Children's National Hospital, Washington, DC 20011, USA
[3]Interdisciplinary Program in Neuroscience, Georgetown University Medical Center, Washington, DC 20007, USA
[4]Laboratory of Comparative Neurobiology, Cavanilles Institute of Biodiversity and Comparative Neurobiology, University of Valencia, CIBERNED-ISCIII, Valencia 46980, Spain
[5]Neuroscience and Cognitive Science Program, University of Maryland, College Park, MD 20742, USA
[6]Department of Cell Biology, Duke University School of Medicine, Durham, NC 27710, USA
[7]Department of Pharmacology & Physiology, Georgetown University Medical Center, Washington, DC 20007, USA
[8]Department of Cell Biology, Functional Biology and Physical Anthropology, University of Valencia, Burjassot 46100, Spain
[9]Center for the Neural Basis of Cognition, University of Pittsburgh, Pittsburgh, PA 15260, USA
[10]Lead contact
*Correspondence: shawn.sorrells@pitt.edu
https://doi.org/10.1016/j.neuron.2023.11.010

SUMMARY

The human amygdala paralaminar nucleus (PL) contains many immature excitatory neurons that undergo prolonged maturation from birth to adulthood. We describe a previously unidentified homologous PL region in mice that contains immature excitatory neurons and has previously been considered part of the amygdala intercalated cell clusters or ventral endopiriform cortex. Mouse PL neurons are born embryonically, not from postnatal neurogenesis, despite a subset retaining immature molecular and morphological features in adults. During juvenile-adolescent ages (P21–P35), the majority of PL neurons undergo molecular, structural, and physiological maturation, and a subset of excitatory PL neurons migrate into the adjacent endopiriform cortex. Alongside these changes, PL neurons develop responses to aversive and appetitive olfactory stimuli. The presence of this homologous region in both humans and mice points to the significance of this conserved mechanism of neuronal maturation and migration during adolescence, a key time period for amygdala circuit maturation and related behavioral changes.

INTRODUCTION

The amygdala is critical for emotional learning and salience discrimination,[1,2] processes that are refined during childhood and adolescence.[3–5] In humans, the amygdala continues to grow significantly in size and mature neuron number between infancy and adolescence.[6–10] This is due in part to the delayed maturation of excitatory neurons in the amygdala paralaminar nucleus (PL).[6,7,11,12] The recruitment of immature PL neurons into established circuits is proposed to influence circuit plasticity[13–16]; however, little is known about the cellular mechanisms underlying this unique form of neuronal development.

The PL was identified in early human histological preparations.[17] PL neurons exhibit immature molecular and morphological features, including expression of doublecortin (DCX)[6,7] and polysialylated neural cell adhesion molecule (PSA-NCAM),[6,11] small nuclei with compacted chromatin, small somas, and few processes.[6] From infancy into adolescence, these immature neurons grow in size and complexity; however, a subpopulation retains immature features in adults as old as 101 years.[18] The PL is prominent in primates adjacent to the basolateral amygdala (BLA),[6,7,12,19–24] and if included with the BLA, in adult humans contains ~20% of BLA neurons.[25] A smaller collection of immature neurons is present adjacent to the BLA in other mammals[26] including sheep,[27] cats[11,28] rabbits,[29] bats,[30] and tree shrews.[31] Whether the experimentally accessible laboratory mouse has a similar PL region has remained unknown.

The presence of immature neurons in the PL raises the question of when these cells are born.[32–34] At birth, the PL already contains immature neurons in humans,[35] and the number of nearby dividing cells declines sharply postnatally, suggesting that the majority of immature PL neurons are born during embryogenesis.[6,8] Interestingly, 5-bromo-2-deoxyuridine (BrdU) birth dating studies in adults found several examples of BrdU co-labeled cells expressing DCX[33] or the neuronal marker NEUN[32] in the non-human primate amygdala and rodent amygdala,[36,37] suggesting they are

Please cite this article in press as: Alderman et al., Delayed maturation and migration of excitatory neurons in the juvenile mouse paralaminar amygdala, Neuron (2023), https://doi.org/10.1016/j.neuron.2023.11.010

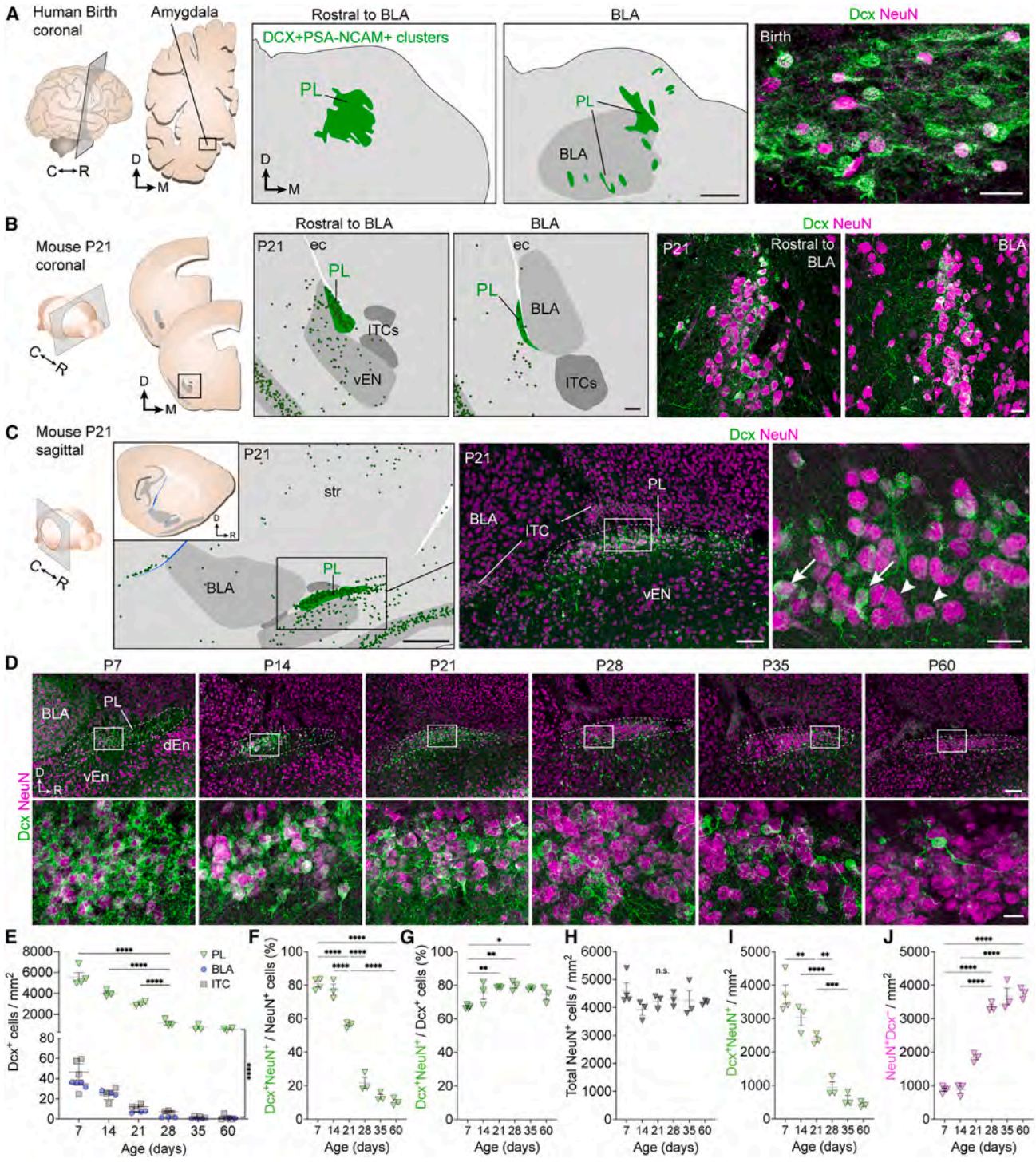

Figure 1. A region with immature neurons in the juvenile mouse amygdala

(A) Human brain coronal maps and Dcx^+NeuN^+ immunostained PL neurons at birth.

(B) Mouse brain coronal maps and Dcx^+NeuN^+ immunostained PL neurons at P21.

(C) Mouse brain sagittal map and immunostaining of Dcx^+NeuN^+ (arrows) or Dcx^-NeuN^+ neurons (arrowheads) at P21.

(D) Age series (P7–P60) of Dcx and NeuN immunostaining in the mouse PL.

(E) Density of Dcx^+ cells within the ITCs, BLA, and PL between P7 and P60.

(F) Percentage of $NeuN^+$ cells in the PL that are Dcx^+ between P7 and P60.

(G) Percentage of Dcx^+ cells in the PL that are $NeuN^+$ between P7 and P60.

(legend continued on next page)

Please cite this article in press as: Alderman et al., Delayed maturation and migration of excitatory neurons in the juvenile mouse paralaminar amygdala, Neuron (2023), https://doi.org/10.1016/j.neuron.2023.11.010

adult-born neurons. These findings require further investigation because dividing glia are closely associated with neurons,[38,39] and dividing oligodendrocyte progenitors (OPCs) in the amygdala[40,41] can express Dcx.[39,42,43] Intriguingly, a subset of PL neurons have a migratory morphology, and migration occurs in known neurogenic regions such as the long-range tangential migration of inhibitory interneurons in the rostral migratory stream (RMS)[44] or the short migration of immature excitatory neurons in the dentate gyrus (DG).[23,24,45] It is unknown whether immature PL neurons with migratory morphology are born postnatally and migrating away from the site of their birth.

In this investigation, we identified the mouse PL based on its morphological, molecular, and developmental similarities to the human PL. We find that in both species, the PL is developmentally and molecularly distinct from adjacent regions: the ventral endopiriform cortex (vEN), which is derived from the lateral pallium and is important in olfaction,[46] or the intercalated cell clusters (ITCs), a primarily GABAergic nucleus derived from the lateral ganglionic eminence (LGE) involved in fear learning.[47–49] We find that the PL is functionally distinct from these adjacent regions, developing selective responses to olfactory stimuli between juvenile and adult ages. Our investigation identifies a conserved developmental mechanism in humans and mice whereby excitatory neurons continue to migrate and grow within established circuits.

RESULTS

Immature mouse PL neurons develop during juvenile ages

To investigate whether the mouse has a homologous region to the human PL, we compared immunostained human and mouse brain sections. In humans at birth, dense clusters of DCX$^+$ immature neurons are adjacent to the BLA in multiple coronal sections (Figure 1A). In mouse coronal sections at postnatal day 21 (P21), we observed Dcx$^+$NeuN$^+$ and Dcx$^+$Psa-Ncam$^+$ cells in a cluster adjacent to the BLA near the ventral terminus of the external capsule (Figures 1B, 1C, S1, and S2A–S2E), which was prominent and more sharply defined in sagittal planes (Figures 1C, S1A, S1B, S1D, and S1E).

To study the timeline of their development, we immunostained immature (Dcx$^+$NeuN$^+$) and mature PL neurons (Dcx$^-$NeuN$^+$) in juveniles (P7–P28), early adolescents (P28–P35), and adults (P60) (Figures 1D–1J). At P7, the PL contained a dense cluster of cells with a meshwork of Dcx labeling that was brighter than surrounding regions (Figure 1D). At all ages from P7 to P60, the density of Dcx$^+$ cells was much higher in the PL than the BLA or ITCs (Figure 1E). The percentage of total PL NeuN$^+$ cells that were Dcx$^+$ significantly declined with age (Figure 1F), and the percentage of Dcx$^+$ cells that were NeuN$^+$ slightly increased (Figure 1G). Total NeuN$^+$ cell density remained constant from P7 to P60 as the density of immature neurons (Dcx$^+$NeuN$^+$) decreased and mature neurons (Dcx$^-$NeuN$^+$) increased (Figures 1H–1J). From this age series, we conclude that similar to the human PL, the mouse PL contains a high density of Dcx$^+$ cells at ages (P7–P14) corresponding to human late gestation and early infancy,[50,51] with a sharp decline during juvenile (P21–P28) and early adolescent ages (P28–P35).

PL neurons are molecularly distinct from adjacent ITC and vEN regions in humans and mice

In mouse brain atlases, the PL region is included either with the main ITC or vEN (see STAR Methods and Figures S1–S3). To distinguish between these regions, we used FoxP2 and Tshz1 to label the dense ITC GABAergic cell clusters that are derived from the Sp8$^+$ LGE[47,48,52,53] and SatB2 to label the vEN.[54] To label the mouse PL, we examined proteins expressed in the human PL[6] including TBR1, a marker of cortical excitatory neurons that implies a PAX6-lineage,[55] COUPTFII, and CTIP2 (see Tables S1 and S2 for a list of abbreviations).

We first visualized the relationship of the mouse PL to neighboring regions in cleared brains stained using iDISCO.[56] The PL contained a high density of Tbr1$^+$ cells close to, but not overlapping with, FoxP2$^+$ cells in the ITCs (Figures 2A, 2B, S2B, S2D, S3A, and S3B; Videos S1 and S2). Between P3 and P120, many Dcx$^+$ PL neurons co-expressed Tbr1, CoupTFII, or Ctip2, but few co-expressed FoxP2, Tshz1, SatB2, Pax6, or Sp8 (Figures 2B, 2C, 2I, and S3B–S3I). Tbr1 was highly expressed (~80%) by both immature (Dcx$^+$NeuN$^+$) and mature (Dcx$^-$NeuN$^+$) PL neurons (Figures 2B–2D). Consistent with overall Dcx$^+$NeuN$^+$ quantifications (Figures 1F, 1G, and 1I), the percentage of Tbr1$^+$NeuN$^+$ cells co-expressing Dcx (Figure 2E) and the density of Dcx$^+$NeuN$^+$ cells co-expressing Tbr1 (Figure 2F) decreased with age. The density of Dcx$^-$NeuN$^+$ cells co-expressing Tbr1 increased significantly with age (Figure 2G), whereas the total NeuN$^+$Tbr1$^+$ density remained constant (Figure 2H). Most (~75%) immature (Dcx$^+$NeuN$^+$) and mature (Dcx$^-$NeuN$^+$) PL neurons expressed CoupTFII at P21, with a significant decrease at P60 (Figures 2I, 2J, S3E, and S3F).

To determine which of these markers label human PL neurons, we stained coronal sections of the PL in human postmortem brain samples at 27 gestational weeks (GWs), birth, 2 years, and 13 years (Figures 2K–2M). We found consistent high co-expression between DCX and TBR1, COUPTFII, or CTIP2 and minimal co-expression of FOXP2 or SATB2 (Figures 2L and 2M). Together, these results reveal transcription factor similarity between the human and mouse PL and a distinction between the PL, ITCs, and vEN in both species.

We next investigated gene expression in mouse PL neurons by microdissecting the region at P22 and performing single-cell RNA sequencing (scRNA-seq) (Figures S4A–S4E). Reclustering only neurons identified multiple clusters that included nearby cortical and striatal neuron subtypes captured in the microdissection (Figures 2N, 2O, and S4D). *Dcx* expression was highest

(H–J) Density of all NeuN$^+$ cells (H) in the PL and the subpopulations that are Dcx$^+$NeuN$^+$ (I) or Dcx$^-$NeuN$^+$ (J).

*p < 0.05, **p < 0.01, ***p < 0.001, ****p <0.0001. One-way ANOVA with Holm-Sidak's test (F–J); two-way ANOVA with Tukey's test (E). Data are mean ± SEM. Scale bars: 2 mm in (A maps); 500 μm in (C, map); 100 μm in (B, maps), (C, middle), and (D, top row); and 20 μm in (A, right), (B, right), (C, right), and (D, bottom row). See also Figures S1–S3.

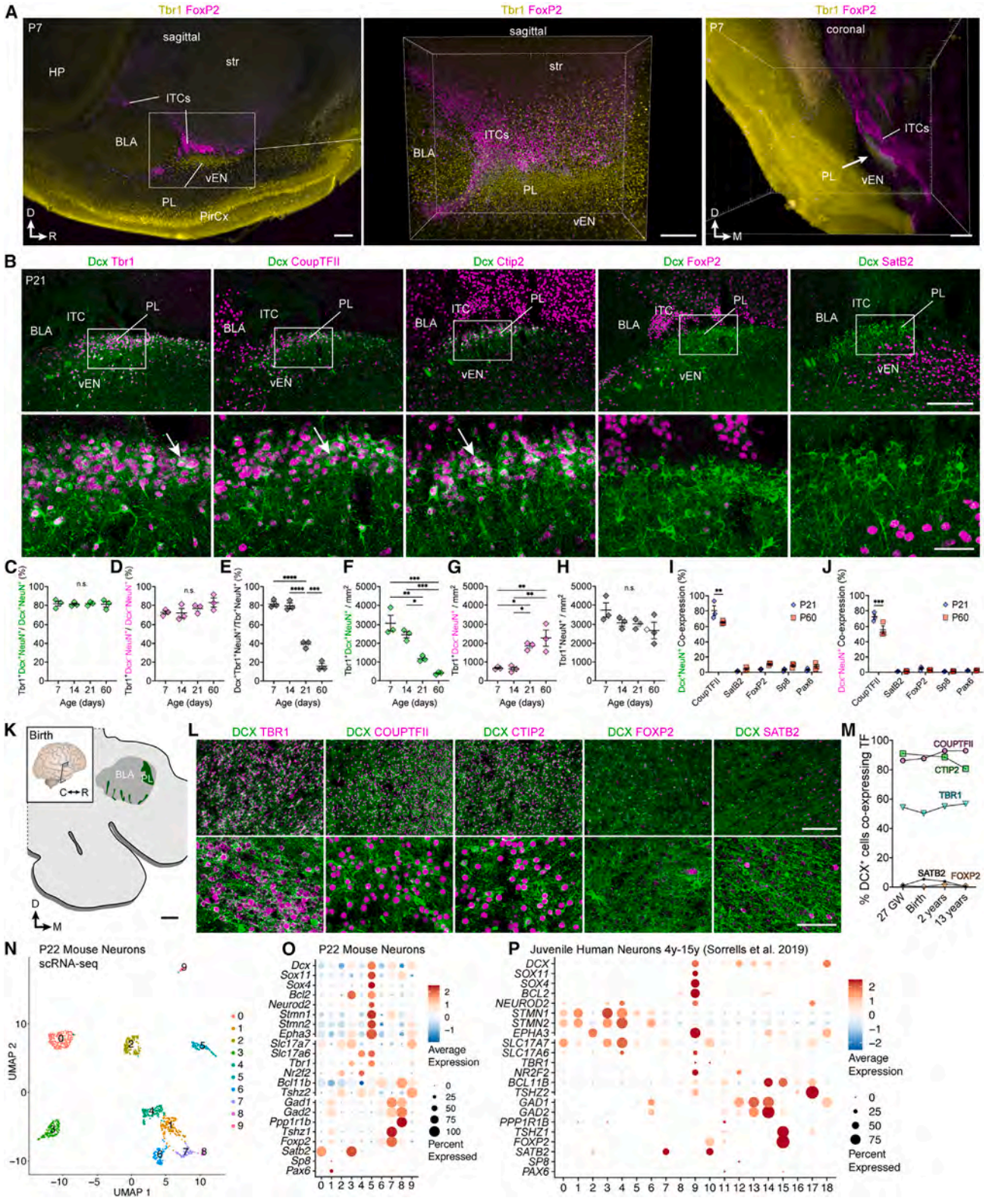

Figure 2. The human and mouse PLs are molecularly distinct from adjacent regions

(A) Cleared P7 mouse brain immunostained for Tbr1 and FoxP2.

(B) Immunostaining of Dcx co-localization with Tbr1, CoupTFII, or Ctip2 (arrows), not FoxP2 or SatB2 at P21.

(legend continued on next page)

Please cite this article in press as: Alderman et al., Delayed maturation and migration of excitatory neurons in the juvenile mouse paralaminar amygdala, Neuron (2023), https://doi.org/10.1016/j.neuron.2023.11.010

in cluster 5, which also highly differentially expressed (DE) multiple immature neuron genes (*Sox11*, *Sox4*, and *Neurod2*) and *Bcl2*, one of the first markers of the PL identified in primates.[22,32] Cluster 5 more weakly expressed some of the regional identity transcription factors (*Nr2f2* [CoupTFII] and *Bcl11b* [Ctip2]), consistent with their lower immunoreactivity in the PL compared with surrounding neurons in the BLA (CoupTFII) and striatum (Ctip2) (Figures 2B and S3B). Cluster 5 expressed markers of excitatory neurons (*Slc17a6*, *Slc17a7*, and *Tbr1*), but not markers of the neighboring inhibitory ITCs (*Gad1*, *Gad2, Foxp2*, and *Tshz1*) or excitatory neurons in the vEN (*SatB2*). Based on these observations, we infer that cluster 5 corresponds to the mouse PL.

We compared these mouse data to our previously published juvenile (4–15 years) human dataset.[6] Reclustering the neurons revealed that only cluster 9 in humans expressed many of the same immature excitatory neuron genes as cluster 5 in the juvenile mouse (Figures 2O, 2P, and S4E–S4H). The genes *Stmn1* and *Stmn2*, which are expressed in immature neurons in primates,[57] were expressed in the immature cluster in mice but were more highly expressed across multiple excitatory neuron clusters in the human (Figure 2P). Overall, cluster 5 in mice and cluster 9 in humans shared many of the same top DE genes compared with other neurons, with 30.3% (93/307) of the mouse genes also DE in humans (Tables S3 and S4). Many of the top DE genes in humans (Table S4) were visible in adult mouse Allen Institute *in situ* and MERSCOPE v1 databases[58] (Figures S4I and S4J). Together, these data reveal a common molecular signature of immature excitatory neurons in the PL of juvenile mice and humans that is distinct from the ITCs or vEN and is consistent with recent transcriptomic identification of PL neurons in adult humans and macaques.[59]

The PL forms during embryonic ages in humans and mice

We previously observed *TBR1*-expressing COUPTFII$^+$ cells in the PL at 22 GWs,[6] suggesting that the human PL forms much earlier than the final gestational months.[35] During mid-gestation, however, immature neurons are ubiquitous, making PL neurons difficult to identify using markers of immaturity. To identify the earliest stages of PL formation in humans, we therefore immunostained for the PL markers TBR1, COUPTFII, and CTIP2, and those of adjacent regions (FOXP2 and SATB2) at progressively earlier ages from 28 GWs to 18 GWs (Figures 3A–3C, S5A, and S5B). At 28 GWs, the PL had a high cellular density compared with the rest of the BLA in a shape similar to the region at birth and was filled with cells expressing TBR1, COUPTFII, or CTIP2, but not SATB2 or FOXP2 (Figures 3A and S5C–S5E). A similar region was identifiable at 22 GWs (Figure 3B); however, the overall heightened density of cells made PL boundaries less sharp. At 18 GWs, we were unable to identify a similar region in rostral sections; however, in two more caudal sections near the temporal lobe lateral ventricle (tLV), the PL markers TBR1, COUPTFII, or CTIP2, but not SATB2 or FOXP2, were expressed in the anatomical location of the PL at older ages (Figures 3C, S5A, and S5B). These data indicate that the human PL forms as early as 18 GWs. We therefore next investigated whether the mouse PL also forms during mid-embryonic ages.

We administered a single dose of BrdU to timed-pregnant females between E12.5 and E16.5 and examined their progeny at postnatal ages (P7, P21, and P35) (Figures 3D–3M and S6A–S6T). At all postnatal ages, the highest percentages of mature (Dcx$^-$NeuN$^+$) PL neurons were born between E12.5 and E14.5 (Figures 3E–3H and S6A–S6D), which was later than mature vEN neurons (Figure 3F). By contrast, the immature Dcx$^+$NeuN$^+$ PL and vEN neurons shared a similar, and later, peak birth date of E14.5 at all postnatal ages (Figures 3I–3M and S6E–S6T). We next examined E16.5 brains to investigate the formation of the PL but did not detect the PL markers Tbr1 or CoupTFII in many cells near the BLA (Figure S7A). By E18.5, however, a dense collection of cells was visible in an anatomical position similar to the PL at older ages. Injection of BrdU at E14.5 revealed many BrdU-labeled cells in this region that were Tbr1$^+$ or CoupTFII$^+$, adjacent to BrdU-negative cells that were SatB2$^+$ or FoxP2$^+$ (Figures 3N and S7B). We crossed *Emx1-Cre* (pallial) and *Gsx2-Cre* (subpallial/pallial-subpallial boundary (PSB)) mice to *ROSA-YFP* reporter mice to label cells derived from these lineages. There was a similar percentage of *Emx1*- and *Gsx2*-derived immature Dcx$^+$ neurons at P21 (Figures S6U–S6X) and mature Tbr1$^+$ neurons at P60 (Figure S6Y), suggesting PL neurons arise from at least two distinct domains in the developing telencephalon. From this, we conclude that the PL forms during embryonic ages in both mice and humans and that immature mouse PL neurons at all postnatal ages share a similar embryonic birthdate and retain Dcx expression for weeks.

Mouse PL neurons are not born from postnatal neurogenesis

To investigate the possibility of postnatal PL neurogenesis, we immunostained for Ki-67 and phosphohistone H3 (pH3). At P3, we observed Ki-67$^+$ or pH3$^+$ cells in the PL that declined by P7 with few at P14 or P21, in contrast to many in the DG (Figures 4A–4G). A low percentage (<1%) of Dcx$^+$ cells were Ki-67$^+$, but in each instance, they also expressed the OPC marker Olig2$^+$ (n = 10/10, Figures 4C and 4E). We observed no

(C–E) Age series (P7–P60) of the percentage of Dcx$^+$NeuN$^+$ cells (C), or Dcx–NeuN$^+$ cells (D) co-expressing Tbr1 and the percentage of Tbr1$^+$NeuN$^+$ cells co-expressing Dcx (E).

(F–H) Density of Tbr1$^+$Dcx$^+$NeuN$^+$ cells (F), Tbr1$^+$Dcx$^-$NeuN$^+$ cells (G), or all Tbr1$^+$NeuN$^+$ cells (H) in the PL between P7 and P60.

(I and J) Percentage of PL Dcx$^+$NeuN$^+$ cells (I) or Dcx$^-$NeuN$^+$ cells (J) co-expressing transcription factors at P21 or P60.

(K–M) Human amygdala map (K) and immunostaining at birth (L), and quantifications of DCX co-expression (M) of each transcription factor from 27 gestational weeks (GWs) to 13 years.

(N) UMAP plot of neuronal clusters from P22 mouse PL microdissection.

(O and P) Dot plots of juvenile mouse (O) or juvenile human (P) neuronal clusters.

*p < 0.05, **p < 0.01, ***p < 0.001, ****p < 0.0001. One-way ANOVA with Holm-Sidak's test (C–H) or two-way ANOVA with Tukey's test (I and J). Data are mean ± SEM. Scale bars: 200 μm in (A), (B, top), and (L, top) and 50 μm in (B, bottom) and (L, bottom). See also Figures S2–S4, Tables S3 and S4, and Videos S1 and S2.

Please cite this article in press as: Alderman et al., Delayed maturation and migration of excitatory neurons in the juvenile mouse paralaminar amygdala, Neuron (2023), https://doi.org/10.1016/j.neuron.2023.11.010

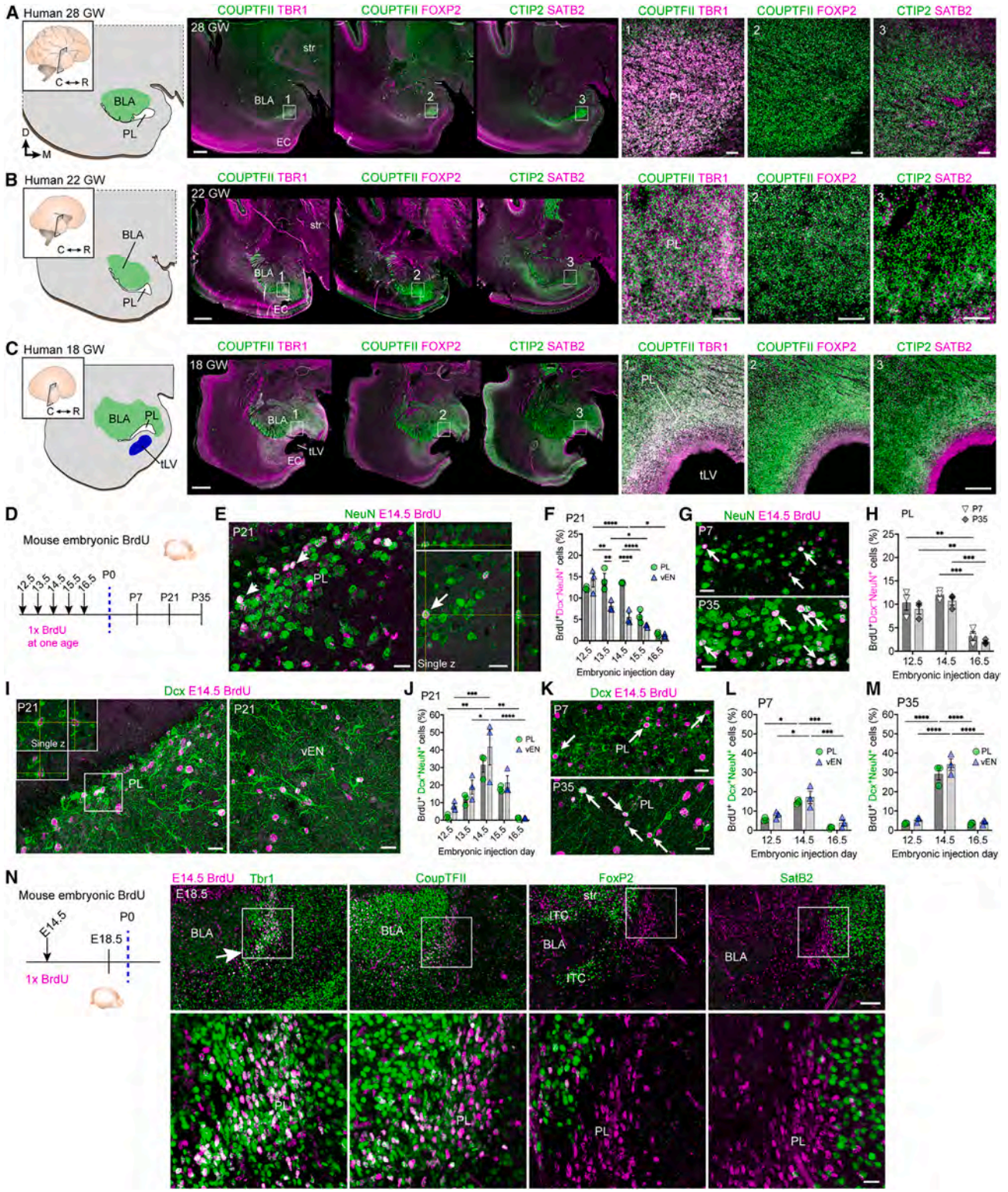

Figure 3. Neurons in the human and mouse PL are born during embryonic ages

(A–C) Human brain coronal maps and sections at 28 gestational weeks (GWs) (A), 22 GWs (B), or 18 GWs (C) stained for COUPTFII and TBR1 (1), COUPTFII and FOXP2 (2), or CTIP2 and SATB2 (3). Boxed insets show the PL region.

(D) Timed-pregnant mice were given BrdU once between E12.5 and E16.5 and offspring were examined at P7, P21, or P35.

(legend continued on next page)

Please cite this article in press as: Alderman et al., Delayed maturation and migration of excitatory neurons in the juvenile mouse paralaminar amygdala, Neuron (2023), https://doi.org/10.1016/j.neuron.2023.11.010

Dcx^+pH3^+ cells in the PL at any age (Figure 4G). We also found minimal PL expression of Tbr2 or Prox1, markers of immature DG excitatory neurons[60,61] in contrast to many labeled cells in the DG (Figures 4H–4M). Together, these observations further support the conclusion that PL Dcx^+ cells are post-mitotic immature neurons.

To further examine the possibility of rare postnatally born immature PL neurons, we administered BrdU postnatally. We first gave P5 mice a single BrdU injection and examined the PL at P7 or P21, but found no BrdU-labeled Dcx^+NeuN^+ or Dcx^-NeuN^+ cells (Figures S8A–S8E). Next, we gave mice BrdU once daily from P10 to P16. We examined BrdU-labeled cells co-stained for Dcx or NeuN in the PL and vEN at P21 (5-day delay) or P35 (19-day delay) to permit time for cellular maturation (Figures 4N and 4O). There were no $NeuN^+$ cells that were BrdU-labeled at either age (Figures 4P–4S). In some instances, BrdU-labeling initially appeared to overlap with NeuN, but orthogonal views of the z stacks showed it was non-overlapping (Figures 4S and S8F–S8I), possibly representing dividing satellite glial cells.[38] A subset of Dcx^+NeuN^- cells had elongated morphologies with a single leading process consistent with migrating neurons. Although migratory neurons would be expected to result from postnatal neurogenesis, these cells were not BrdU-labeled (Figures 4T and 4U) and instead had an embryonic birthdate similar to other Dcx^+ PL neurons (Figures S6I–S6T).

Within the BrdU-labeled population, we observed a low frequency (~1.3%) of NeuN-negative cells that were lightly immunoreactive for Dcx (Figures 4V–4X). The percentage and density of these cells were constant in the PL and vEN at both ages, their small, round, and multipolar morphology was similar to that of OPCs, and 100% co-expressed Olig2 (Figures 4Y–4AA; total across 45 sections/n = 9 mice: n = 18 PL cells n = 147 vEN cells). Between P3 and P60, a small subset of PL Dcx^+ cells expressed Olig2 or adenomatous polyposis coli (APC) (Figures S8J–S8U), agreeing with prior observations of Dcx expression in OPCs.[39,41–43,62] At P21, Dcx-immunogold-labeled cells in the PL could be observed with ultrastructural features distinctive of either oligodendrocytes or immature neurons (Figure S8K). Consistently, in our P22 scRNA-seq, we observed OPC clusters expressing *Olig2* and *Dcx* (Figure S4C) but no clusters defined exclusively by markers of radial glia (e.g., *Vim*, *Nes*, *Hopx*, and *Mki67*). Together, these results support the conclusion that PL and vEN neurons are born during embryonic ages, not from postnatal neurogenesis.

Local maturation of mouse PL neurons occurs during juvenile ages

We next used transmission electron microscopy to study the ultrastructure of PL neurons. At P21, the PL is composed of a dense collection of large and small neurons (Figures 5A and 5B). The smaller neurons had compacted chromatin, limited cytosol, and few organelles other than ribosomes. Interestingly, a subset of these cells had features typical of migratory neurons including Dcx-immunogold-labeled expansions, intercellular spaces, and zonula adherens-like contacts. Intermediate-size neurons had more cytosol and organelles but retained some compacted chromatin, appearing as an intermediate stage of maturation. The largest PL neurons received axosomatic synapses containing pleomorphic vesicles and more mitochondria and endoplasmic reticulum. These results show that P21 PL neurons have ultrastructural features consistent with progressive stages of growth.

To further investigate their maturation, we used patch-clamp electrophysiology to record from PL neurons in acute brain slices between P21 and P28. We recorded from neurons that fired rudimentary action potentials with small amplitudes and long durations and neurons that fired robust action potential trains with greater efficiency (Figure 5C). We defined the subset with immature action potentials based on high resistance (>1 GΩ), depolarized threshold (>−35 mV), and long spike duration (>5 ms) (Figure 5D). These immature neurons were present across all ages examined (Figure 5E), and compared with all other recorded neurons, they exhibited significantly depolarized resting membrane potential, longer time constant, and smaller spike amplitude and no difference in capacitance, rheobase current, or depolarization/repolarization ratio (Figure 5F). We detected spontaneous excitatory postsynaptic currents (sEPSCs) in 3/5 immature neurons and 18/20 mature neurons, and spontaneous inhibitory postsynaptic currents (sIPSCs) in 1/5 immature neurons and 6/20 mature neurons. The frequency and amplitude of these spontaneous input currents were similar between the immature and mature groups (Figure 5G). These data show that the juvenile PL (P21–P28) contains neurons with physiological properties that reflect different stages of maturity.

We filled a subset of recorded neurons (n = 18) with biocytin to visualize their morphology and immunostain for Dcx. All Dcx^+-filled neurons had physiologically immature properties; however, we observed both simple and complex morphologies within this group (Figure 5H), suggesting that their morphological complexity may increase before Dcx protein expression is lost. The Dcx^+ neurons with more complex morphology fired a greater number of action potentials with larger amplitudes at rheobase and fell closer to the mature side of the physiological continuum compared with those with simple morphology (e.g., cell 2 in Figure 5D). Together, these data reveal that the juvenile PL (P21–P28) contains neurons with a broad range of ultrastructural, morphological, and physiological indicators of maturity.

(E–H) $BrdU^+NeuN^+$ cells in the PL at P21 (arrows, E) or P7 and P35 (G) after an E14.5 injection. Quantification of Dcx^-NeuN^+ cell $BrdU^+$ percentage in the PL and vEN at P21 (F), or the PL at P7 and P35 (H).

(I–M) $BrdU^+Dcx^+$ co-localized cells in the PL and vEN at P21 (I), or the PL at P7, and P35 (K) after an E14.5 injection. Quantification of Dcx^+NeuN^+ cell $BrdU^+$ percentage in the PL and vEN at P21 (J) and at P7 (L) and P35 (M).

(N) At E18.5, $BrdU^+Tbr1^+$ cells and $BrdU^+CoupTFII^+$ cells are present (boxed insets) between $BrdU^-FoxP2^+$ and $BrdU^-SatB2^+$ regions, after an E14.5 BrdU injection, with some emanating into the cortex (arrow).

*p < 0.05, **p < 0.01, ***p < 0.001, ****p < 0.0001. Two-way ANOVA with Tukey's test. Data are mean ± SEM. Scale bars: 2 mm in (A)–(C, left); 500 μm in (C 1–3, right); 100 μm in (A 1–3 right), (B 1–3 right), and (N top); 20 μm in (E), (G), (I), (K), and (N bottom). See also Figures S5–S7.

Please cite this article in press as: Alderman et al., Delayed maturation and migration of excitatory neurons in the juvenile mouse paralaminar amygdala, Neuron (2023), https://doi.org/10.1016/j.neuron.2023.11.010

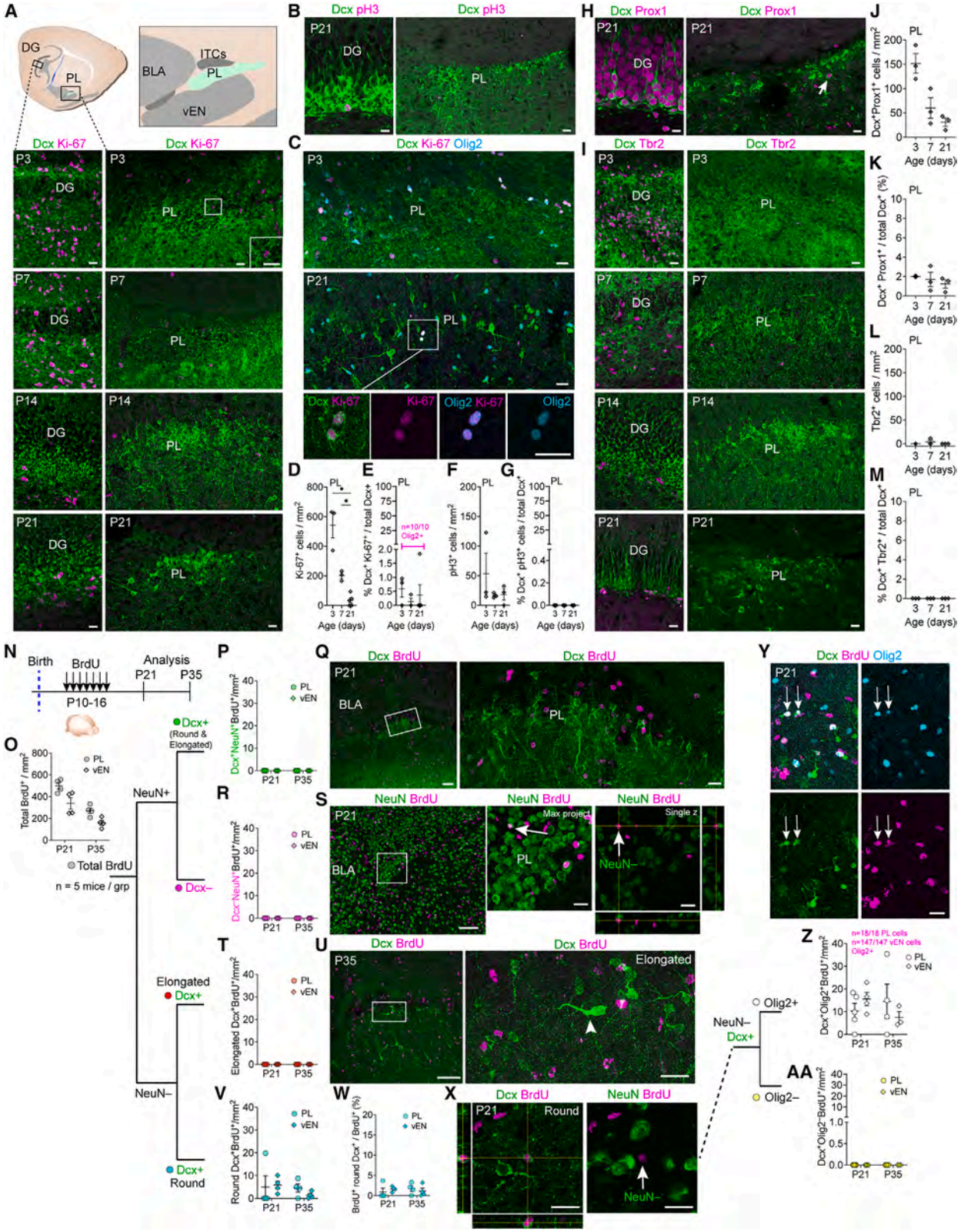

(legend on next page)

Please cite this article in press as: Alderman et al., Delayed maturation and migration of excitatory neurons in the juvenile mouse paralaminar amygdala, Neuron (2023), https://doi.org/10.1016/j.neuron.2023.11.010

Not all mouse PL neurons mature locally during juvenile ages

To track the fate of Dcx$^+$ PL neurons after they lose Dcx expression, we crossed *Dcx-CreER*™ mice to a *ROSA-LSL-tdTomato* (tdT) reporter. We observed expected tamoxifen (TMX)-induced tdT recombination in the Dcx$^+$ cells in the RMS, ventricular-subventricular zone (V-SVZ), and olfactory bulb as well as the PL and piriform cortex (Figures 6A–6E and S9A–S9F). We administered TMX either before the sharp decrease (Figures 1F and 1I) in Dcx$^+$ cells (P21–P23, Figures 6A–6C) or after the decrease (P28–P30, Figures 6A and 6D) and analyzed brains after 2, 5, or 12 days. We observed tdT$^+$Dcx$^+$Tbr1$^+$ cells with a range of morphologies from simple to complex in the PL and vEN at every age (Figures 6B–6D and S9C–S9F). In the P21–P23-labeled PL, the percentage of tdT$^+$ cells that were Dcx$^+$ decreased with time post-TMX; however, P28–P30-labeled PL tdT$^+$ cells remained Dcx$^+$ (Figure 6E). This suggests that prior to P28, many Dcx$^+$ PL neurons downregulate Dcx expression as they transition to maturity, whereas after P28, Dcx expression is preferentially retained.

We next used unbiased stereology to estimate total cell numbers in the PL and vEN between P7 and P60 to determine whether migration of the PL Dcx$^+$ neurons with elongated morphology into the vEN contributes to the overall decline in Dcx$^+$ PL neurons (Figures 6F–6N; Tables S5 and S6). The PL Dcx$^+$ population (Figures 6F and 6G) was ~12,000 cells at P7, decreasing by 21.3% at P21, before sharply dropping by 63.6% between P21 and P28 and reaching a plateau of ~2,000 Dcx$^+$ cells between P35 and P60. This was similar to the timeline in Figures 1F and 1I and represented a total PL Dcx$^+$ cell decrease of ~10,000 between P7 and P60. The total number of DAPI$^+$ PL nuclei also slightly decreased between P7 and P60, dropping by ~2,000 (Figures 6L and 6M). PL NeuN$^+$ cells actually increased by ~2,000 from P7 to P21 (Figures 6I and 6J), consistent with the timing of NeuN upregulation as Dcx$^+$ cells mature (Figure 1J). Interestingly, however, in the vEN, there was a sharp increase from ~2,000 Dcx$^+$ cells at P7–P14 to ~7,000 at P21, which remained higher from P28 to P35, before falling by P60 (Figure 6H). Similarly, the total number of vEN DAPI$^+$ nuclei was relatively constant from P7 to P14 before sharply increasing by ~10,000 at P21 and remaining stable into adulthood (Figure 6N). The total number of vEN NeuN$^+$ cells was also relatively constant between P7 and P21 until P28 when it increased by ~5,000 (Figure 6K). The overall decrease in Dcx$^+$ cells in the PL and corresponding increases in the vEN around the same ages (P21–P28) support the conclusion that a subset of PL Dcx$^+$ cells migrate into the vEN.

Because the developmental timeline of PL neurons is delayed, we predicted that their developmental programmed cell death might also be delayed to occur during the peak decline of Dcx$^+$ cells (P21–P28). We immunostained for cleaved-caspase-3 (CC3)[63] and found that the peak of PL and vEN CC3 expression occurred at ages typical for cortical neurons (P3–P7)[64,65] (Figures 6O–6R, S10A, and S10B). Between P14 and P28, the PL had at most 1–2 CC3$^+$ cells per hemisphere. Together, these findings indicate that reduced Dcx$^+$ and NeuN$^+$ PL cell numbers are not the result of a delayed wave of caspase-dependent programmed cell death and are largely driven by Dcx downregulation with maturation or migration.

Tbr1$^+$ neurons with migratory morphology emanate from the mouse and human PL in juvenile ages

To investigate the molecular identity of the migratory neurons, we next immunostained for the PL marker Tbr1 alongside Sp8, which labels interneurons in the RMS.[53] Nearly all Dcx$^+$ cells with migratory features like elongated nuclei and a single leading process were Tbr1$^+$, with Dcx$^+$Sp8$^+$ cells primarily observed in medial sections near the RMS (Figures 7A, S10C, S10D, S11A, and S11B). We observed similar elongated cells with migratory features in the Dcx-CreER™;tdT-reporter mice given TMX at either age (Figures 6C, 6D, and 7B), in Dcx-mRFP mice (Figure S11C), and ultrastructurally (Figures 7C, 7D, S11D, and S11E).

We mapped the location and morphology of Dcx$^+$ neurons in the PL and vEN between P7 and P60 (Figures 7E and S11F–S11I). Migratory Dcx$^+$Tbr1$^+$ cells were present at every age, increasing between P21 and P28 to 6%–7% of all Dcx$^+$ cells in the PL and 30% in the vEN compared with <1% that were Sp8$^+$ (Figure 7F). Their leading processes were primarily oriented radially between the vEN and the PL (Figure 7E). These cells decreased by P35–P60, and we detected few Dcx$^+$ cells with elongated morphology near the piriform cortex or BLA or entering the PL from other nearby areas (Figures 7E and S11F–S11K).

To further investigate PL migration, we imaged acute slices from Dcx-mRFP mice at P2–P3 with confocal microscopy

Figure 4. Neurons in the mouse PL are not born postnatally

(A and B) (A) Mouse sagittal map and immunostaining in the DG and PL for Dcx and Ki-67, and (B) for Dcx and pH3.

(C) Immunostaining of a PL Dcx$^+$Ki-67$^+$Olig2$^+$ pair (inset).

(D–G) Quantification of PL Ki-67$^+$ (D) or pH3 (F) cell density and percentage of Dcx$^+$ cells that were Ki-67$^+$ (E) or pH3$^+$ (G).

(H) Immunostaining of a PL Dcx$^+$Prox1$^+$ cell (arrow).

(I) Immunostaining of Dcx and Tbr2.

(J–M) Quantification of PL Dcx$^+$Prox1$^+$ cell density (J) and percentage of Dcx (K), and PL Tbr2$^+$ cell density (L) and percentage of Dcx (M).

(N) Experimental design for postnatal BrdU P10–P16.

(O) Total BrdU$^+$ density.

(P–X) Quantifications (P, R, T, V, and W) and immunostaining (Q, S, U, and X) of cell populations co-stained with BrdU. Putative NeuN$^+$BrdU$^+$ cells (arrows) were determined with orthogonal views to be single-positive (S). Example of elongated Dcx$^+$ neuron (arrowhead) that is BrdU negative (U). Example of round Dcx$^+$ NeuN-negative cell (X) that is BrdU$^+$ (arrow).

(Y–AA) Immunostaining of a Dcx$^+$BrdU$^+$Olig2$^+$ pair (Y, arrows) in the PL and quantification of Dcx$^+$BrdU$^+$Olig2$^+$ cell density (Z) and Dcx$^+$BrdU$^+$Olig2$^-$ cell density (AA).

*$p < 0.05$, one-way ANOVA with Holm-Sidak's test (D). Data are mean ± SEM. Scale bars: 100 μm in (Q left), (S left), (U left) and 20 μm in (A)–(C), (H), (I), (Q right), (S middle and right), (U right), (X), and (Y). See also Figures S4 and S6–S8.

Please cite this article in press as: Alderman et al., Delayed maturation and migration of excitatory neurons in the juvenile mouse paralaminar amygdala, Neuron (2023), https://doi.org/10.1016/j.neuron.2023.11.010

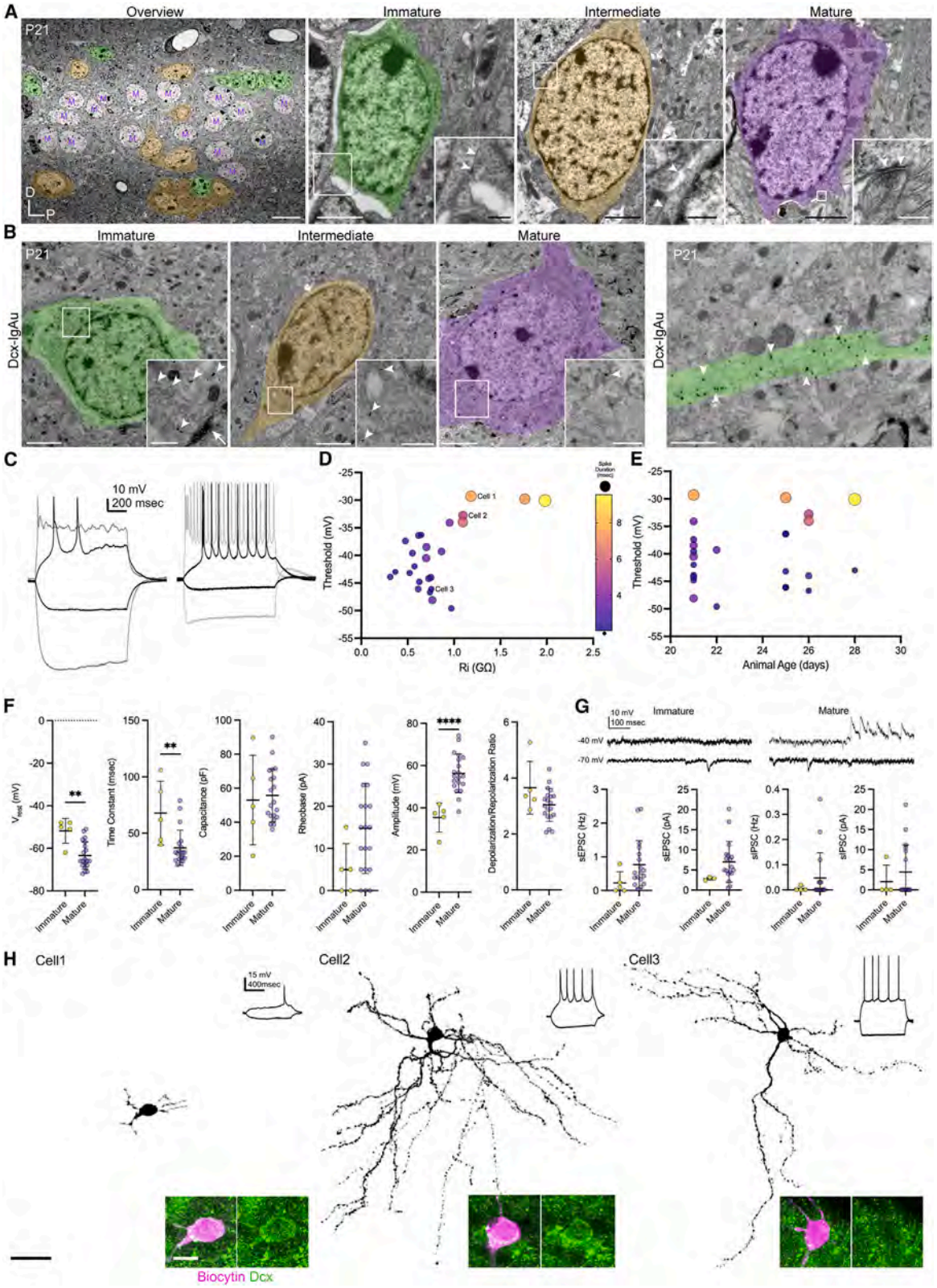

(legend on next page)

Please cite this article in press as: Alderman et al., Delayed maturation and migration of excitatory neurons in the juvenile mouse paralaminar amygdala, Neuron (2023), https://doi.org/10.1016/j.neuron.2023.11.010

(Figures 7G–7N; Video S3). Many migratory mRFP$^+$ cells originated in the PL and extended their leading process into the neighboring vEN (Figures 7G–7J). One PL mRFP$^+$ cell was stationary for 24 h of imaging before migrating into the vEN (Figure 7I). Another mRFP$^+$ cell extended its leading process into the PL, reoriented toward the vEN, and bifurcated its leading process multiple times before settling after 48 h (Figure 7N). We estimated the speed and distance (Figures 7J–7M) of radially or tangentially migrating neurons, orientations typical of excitatory or inhibitory interneurons, respectively.[66,67] The majority of neurons emanating from the PL were migrating radially with an average speed of 13.8 μm/h (±10.5 μm/h, SD), similar to previous measurements of excitatory neurons.[68,69] Through post hoc immunostaining, we found that the majority of mRFP$^+$ neurons with elongated morphology were Tbr1$^+$ not Sp8$^+$ (Figure 7O). Together with the timing of total cell population changes in the PL and vEN (Figures 6F–6N), these observations indicate that a subpopulation of Dcx$^+$Tbr1$^+$ neurons migrate from the PL into the vEN during postnatal ages with evidence of a delayed wave between P21 and P35.

We next examined human PL neurons and found many DCX$^+$ cells with a similar elongated morphology expressing the PL markers TBR1$^+$COUPTFII$^+$ or CTIP2$^+$SATB2$^-$ at 13 years (Figure 7P). Quantification of putative migratory DCX cells across postnatal ages from 2 to 24 years identified a peak in their abundance and density at 6 years (Figures 7Q and 7R). Consistent with prior observations,[6] these cells were oriented either toward the accessory basal amygdala or along the white matter tracts ventral to the PL.

The mouse PL develops selective responses to olfactory stimuli between juvenile and adult ages

To explore stimuli that activate the PL, we investigated the PL response in juvenile (P25–P27) and adult (P60–P100) mice to odorants known to activate the ITCs and vEN. The ITCs are important for fear learning and are activated by aversive stimuli such as the odor of a predator,[47–49] whereas the vEN plays an important role in odorant information processing.[70] We immunostained the PL for Dcx and the immediate early gene (IEG) c-Fos, following presentation of odorants in a tube containing aversive (bobcat urine,[71] predator odor (PO)), appetitive (novel food, FO), or novel non-food (NO) odorants, or mineral oil (MO) (Figures 8A and 8E). There was a significant (2-fold) c-Fos$^+$ cell increase following PO exposure within the adult ITCs, but not in juvenile ITCs, or at either age in the PL or vEN (Figures 8B–8D). By contrast, the adult PL and vEN displayed a significant (~2-fold) c-Fos$^+$ cell increase following either FO or NO exposure that was not present in the juvenile PL or vEN, in the ITCs following any condition, or following MO in any age or brain region (Figures 8F–8H). These data indicate that between juvenile and adult ages, the PL and vEN develop a response to appetitive and novel olfactory stimuli, whereas the ITCs develop a response to aversive stimuli.

Interestingly, there were also Dcx$^+$c-Fos$^+$ cells in the PL and vEN following these stimuli, including both small, simple cells and large, complex cells with multiple immunoreactive branching dendrites (Figures 8I–8O). The total number of Dcx$^+$c-Fos$^+$ cells in the PL and vEN was higher following PO or FO compared with MO controls (Figures 8J and 8M), even at juvenile ages when each region was less responsive (Figures 8C, 8D, 8G, and 8H). Similarly, the percentage of all PL Dcx$^+$ cells that were c-Fos$^+$ (up to 5%–10%) increased following PO or FO, but the vEN Dcx$^+$ cells responded more to FO or NO (Figures 8K, 8L, 8N, and 8O). We investigated co-expression of other IEGs and found no Arc expression in the PL, but found a similar percentage of Dcx$^+$ cells labeled with Egr1 in the juvenile following FO (8.9% c-Fos$^+$Dcx$^+$ vs. 9.3% Egr1$^+$Dcx$^+$ cells). Together, these data suggest that the juvenile PL lacks the responses to odorants that emerge in adults, yet immature PL neurons already exhibit responsiveness to aversive and appetitive odors in juveniles.

DISCUSSION

Here we show that the mouse has a previously undescribed non-neurogenic region with immature excitatory neurons that is homologous to the human PL. In humans, PL neurons are hypothesized to undergo delayed maturation, migration, and functional integration into nearby circuits. In mice, we find that PL neurons undergo delayed maturation across ultrastructural, morphological, and electrophysiological criteria. Mouse PL neurons also migrate into the vEN, peaking during juvenile ages concurrent with emerging functional responses of PL neurons.

The presence of Dcx$^+$ neurons is often interpreted as evidence of neurogenesis.[72,73] Immature neurons are present in well-described adult neurogenic regions in the mouse DG[74,75] and

Figure 5. Maturation of mouse PL neuron morphological and physiological properties in juvenile ages

(A and B) Ultrastructure of PL neurons: immature (green), intermediate (yellow), and mature (M, magenta). Immature neurons have intercellular space, zonula adherens-like contacts (A, immature and intermediate inset arrowheads), compacted chromatin (B, arrow), and Dcx-immunogold labeling (B, arrowheads). Mature PL neurons receive axosomatic synapses (A, mature inset arrowheads) with pleomorphic vesicles, more organelles, and less heterochromatin and Dcx labeling. Dcx-immunogold labeling (B, right arrowheads) in a cell expansion (green).

(C) Immature (left) and mature (right) action potentials at rheobase (black) and rheobase + 30 pA (gray).

(D and E) Threshold and spike duration plotted against input resistance (D) or animal age (E).

(F) Electrical properties of immature and mature PL neurons.

(G) Spontaneous inhibitory postsynaptic current (sIPSC) and spontaneous excitatory postsynaptic current (sEPSC) example traces (top) and frequency/amplitude comparisons (bottom).

(H) Representative biocytin-filled morphologies from (D) and their current clamp traces (top right). Insets, immunostaining for Biocytin Dcx$^+$ (cells 1 and 2) and Dcx$^-$ (cell 3) somas.

*p < 0.05, **p < 0.01, ****p < 0.0001. Data are mean ± SD. Unpaired t test with Shapiro-Wilk normality test. Scale bars: 30 μm in (H overview), 10 μm in (A left overview) and (H, inset), 2 μm in (A right) and (B), 1 μm in (B mature inset, right), 500 nm in (A) and (B immature and intermediate insets), and 200 nm in (A mature inset).

Please cite this article in press as: Alderman et al., Delayed maturation and migration of excitatory neurons in the juvenile mouse paralaminar amygdala, Neuron (2023), https://doi.org/10.1016/j.neuron.2023.11.010

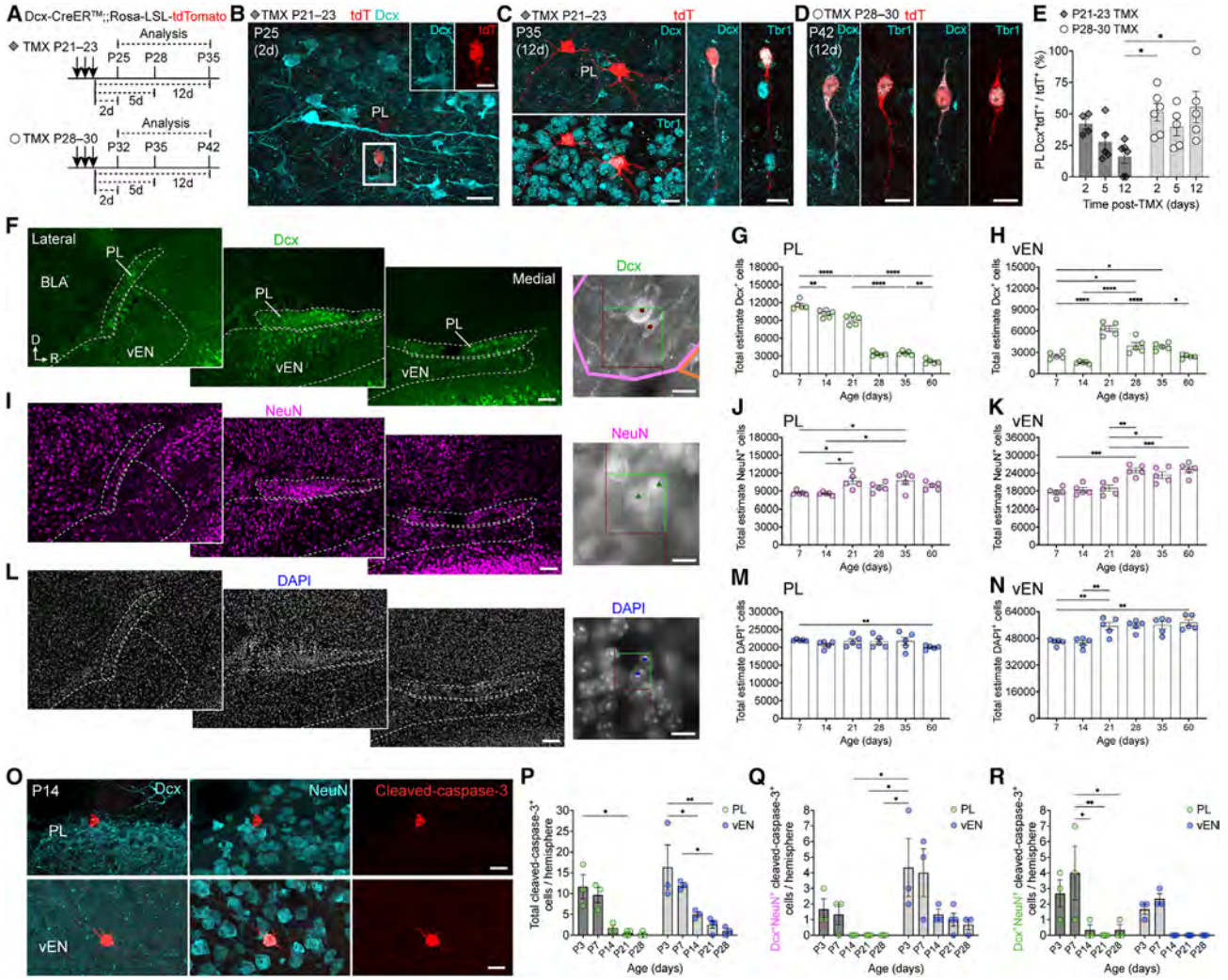

Figure 6. Dcx$^+$ mouse PL neurons either retain Dcx expression, downregulate Dcx with maturation, or migrate into the vEN

(A) Experimental design for (B)–(E).

(B–E) Examples of simple (B and D) and complex (C) tdT$^+$Dcx$^+$ cell morphology and (E) quantification of the percentage of tdT$^+$ cells co-expressing Dcx.

(F–N) Stereological measurements of Dcx$^+$ cells (F–H), NeuN$^+$ cells (I–K), and DAPI$^+$ nuclei (L–N) between P7 and P60. PL boundaries at 3 sagittal levels immunostained for Dcx (F), NeuN (I), and DAPI (L) showing representative counted objects. Estimates of total cell populations for Dcx$^+$ cells in the PL (G) and vEN (H), for NeuN$^+$ cells in the PL (J) and vEN (K), and for DAPI$^+$ cells in the PL (M) and vEN (N) between P7 and P60.

(O) Immunostaining of CC3$^+$ cells in the PL (Dcx$^-$ and NeuN$^-$) and vEN (Dcx$^-$ and NeuN$^+$).

(P–R) Quantifications of CC3$^+$ (P), Dcx$^-$NeuN$^+$CC3$^+$ (Q), and Dcx$^+$NeuN$^+$CC3$^+$ cells (R).

*p < 0.05, **p < 0.01, ***p < 0.001, ****p < 0.0001, one-way (G, H, J, K, M, and N) or two-way ANOVA (E, P, Q, and R) with Holm-Sidak's test (E, G, H, J, K, and N), Dunnett's test (M), or Tukey's test (P–R). Data are mean ± SEM. Scale bars: 100 μm in (F, left), (I, left), and (L, left); 20 μm in (B, overview), (C, left), and (O); 10 μm in (B, inset), (C, right), (D), (F, right), (I, right), and (L, right). See also Figures S9–S11 and Tables S5 and S6.

SVZ[44] and in the non-neurogenic adult piriform cortex.[15,76–78] Our results show that the Dcx$^+$ cells in the PL and vEN have an embryonic birthdate, with no indications of postnatal neurogenesis, suggesting these cells are developmentally arrested and mature at later postnatal ages. Delayed neuronal maturation has been proposed[79] to explain the DCX$^+$ cells with mature morphologies[80] in the human hippocampus in the absence of dividing neural progenitor cells.[72,81,82] Our findings show that across species, the late maturation of excitatory neurons and their continued recruitment can occur in the absence of neurogenesis, providing a mechanism to shape the processing of information well into postnatal life.

As PL neurons mature, they undergo similar changes in excitability and firing efficiency but exhibit different synaptic input properties compared with adult-born immature neurons in the DG and non-adult-born immature neurons in the piriform cortex. In all three regions, maturing neurons decrease input resistance, hyperpolarize resting membrane potential and threshold, and increase action potential amplitude and speed.[15,76,83] The remarkably complex morphology of some Dcx$^+$ PL neurons is similar to

Please cite this article in press as: Alderman et al., Delayed maturation and migration of excitatory neurons in the juvenile mouse paralaminar amygdala, Neuron (2023), https://doi.org/10.1016/j.neuron.2023.11.010

CellPress

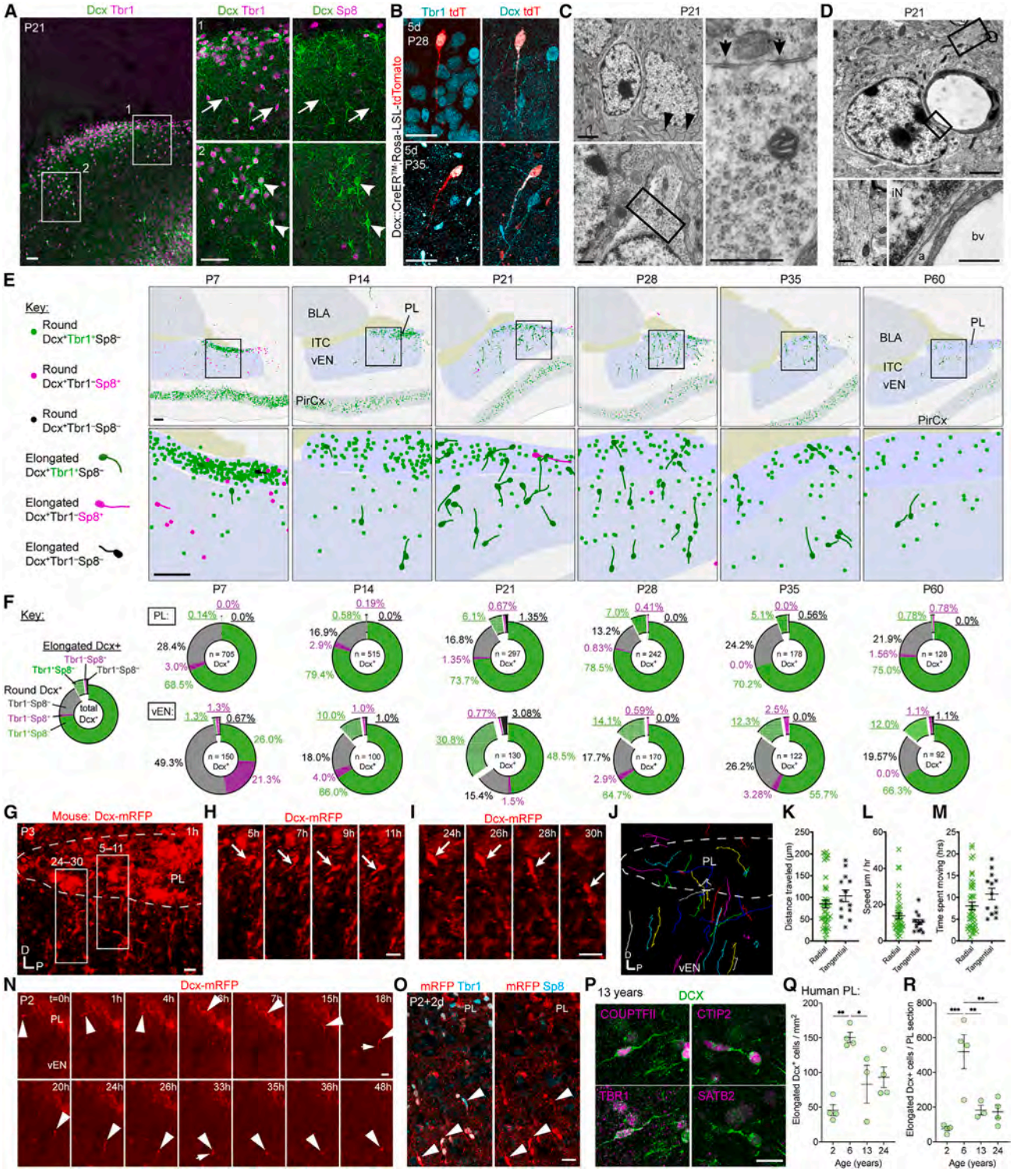

Figure 7. Mouse PL Tbr1$^+$ neurons migrate into the vEN from birth into early adolescence

(A) Immunostaining of rounded/complex (arrowheads) and elongated (arrows) Dcx$^+$Tbr1$^+$Sp8$^-$ cells at P21.

(B) Elongated Dcx-CreER™-tdT$^+$Dcx$^+$Tbr1$^+$cells.

(C) Fusiform neuron with migratory ultrastructural characteristics: compacted chromatin, elongated nucleus and cell body, few organelles aside from ribosomes (inset), intercellular spaces, and cell-cell contacts (arrows). Adjacent mature neuron with long endoplasmic reticulum (black arrowheads).

(D) Immature neuron (iN) ultrastructure showing an expansion with microtubules (inset) near an astrocytic process (a) and a blood vessel (bv).

(legend continued on next page)

Please cite this article in press as: Alderman et al., Delayed maturation and migration of excitatory neurons in the juvenile mouse paralaminar amygdala, Neuron (2023), https://doi.org/10.1016/j.neuron.2023.11.010

observations in the piriform cortex[15,76] and underlines that Dcx expression is insufficient to indicate immaturity. The synaptic input properties of PL neurons, by contrast, are distinct from the piriform and dentate. In these other regions, GABA inputs predominate in immature neurons, and in the DG excitatory, GABA is important for neuronal maturation.[84,85] In immature PL neurons, we observed both excitatory and inhibitory synaptic currents with no differences in frequency or amplitude compared to mature neurons, suggesting that between P21 and P28, PL physiological maturation does not coincide with significant development of synaptic inputs. It will be interesting to investigate the source(s) of this input to the PL and their interactions with maturing PL neurons at other ages.

Our data reveal an increase in the prominence of PL neurons in the human amygdala compared with mice. The ratio of PL to BLA neurons is ~1:4 in humans,[25] compared with ~1:9 in mice,[86] or ~2-fold increase in relative neuron number. The location of the PL relative to the BLA is also extended in primates, sheep, and cats[11,19,27] with a greater caudal extension compared with its rostral position in lissencephalic species like bats[87] tree shrews,[31] and, as we now show, in mice. The location of the vEN is debated in primates[46]; however, some atlases place it between the rostral PL and piriform cortex, a region where immature neurons appear to extend from the PL,[6,22] similar to our observations in mice. Cortical expansion and increasing PL size may have resulted in the position of the PL being extended along the BLA in primates so that migratory cells enter the BLA compared with the vEN in mice. In both species, the PL neurons likely migrate relatively short distances as they are primarily found near the PL[6,7,11,19] and do not have high levels of Dcx expression or elongated nuclei in chain migration.[88] The PL region has been described as a migratory reservoir in gestational rats[89] at the ventral extent of the lateral cortical migratory stream, which follows the external capsule.[90,91] Our time-lapse recordings suggest that migratory PL Tbr1$^+$ excitatory neurons may be a continuation of these embryonic migratory routes. Section viability limited our live imaging in older ages; however, PL Tbr1$^+$ cells were not observed in the RMS, striatum, BLA, or any cortical layers aside from the piriform cortex. We cannot exclude the possibility that a small subpopulation enters the amygdala cortical or dorsal endopiriform regions.

The location of the PL near the amygdala and olfactory brain regions makes it well positioned to respond to emotional, social, and/or survival cues. PL responses to olfactory stimuli were significantly greater in adults than in juveniles, suggesting that PL functionality emerges after the peak period of migration and maturation. Surprisingly, however, the immature neurons in the juvenile PL and vEN exhibited a similar response to appetitive and aversive olfactory stimuli, suggesting the possibility of a shared function that is different from each region as a whole. Although these results show PL neuron responsiveness to olfactory stimulation, they do not yet define a functional role for these cells in behavior, and it will be interesting to uncover their importance in appetitive and/or aversive behavioral responses as animals enter and emerge from adolescence.

The introduction of new neurons into developing or established networks is an important form of neuron structural plasticity.[13,92,93] This can occur from adult neurogenesis, which in the rodent hippocampus supports processes such as cognitive flexibility and learning[94]; however, most brain regions do not continue to produce newly born neurons, especially in mammalian species with large brains.[14,72,92,95–98] PL neurons develop during critical ages for adolescent socioemotional development.[7,8,99] Almost half of all lifetime mental health conditions onset during mid-teenage years,[100] and changes in amygdala volume and development are linked to social and emotional disorders.[7,101–105] PL neurons are beginning to be investigated in human neuropsychiatric conditions including autism spectrum disorder,[7] epilepsy,[106] and major depressive disorder,[107] suggesting our findings may have broad implications for understanding cellular and molecular mechanisms underlying amygdala-linked disorders. The identification of the PL in both mice and humans further points to the significance of this conserved cellular mechanism of neuron recruitment and migration during juvenile life and adolescence, key ages for amygdala circuit maturation and accompanying behavioral changes.

STAR★METHODS

Detailed methods are provided in the online version of this paper and include the following:

- KEY RESOURCES TABLE
- RESOURCE AVAILABILITY
  - Lead contact
  - Materials availability
  - Data and code availability
- EXPERIMENTAL MODEL AND STUDY PARTICIPANT DETAILS
  - Mice
  - Human postmortem tissue
- METHOD DETAILS
  - 5-bromo-2-deoxyuridine (BrdU) administration
  - Tamoxifen (TMX) administration
  - Mouse tissue immunostaining
  - Anatomical boundaries of the developing and adult mouse paralaminar nucleus
  - Unbiased stereology

(E and F) Maps (E) and quantifications (F) of round and elongated Dcx$^+$ cells expressing Tbr1, Sp8, or neither between P7 and P60.
(G–O) Acute slice time-lapse imaging of P2–P3 Dcx-mRFP mice. Initial time-lapse field (G), a cell extending from the PL into the vEN (arrow, H), and a previously stationary cell beginning to migrate (arrow, I). Traces of the migratory paths (J) over a 30 h period. (K–M) Total distance traveled (K), speed (L), and time traveled (M) average of n = 3 independent recordings (P2–P3). Dcx-mRFP$^+$ cell (N) migrating into the PL (arrowhead), re-orienting (t = 7 h), bifurcating its process (arrows, t = 18 h, t = 33 h) then settling (t = 35–48 h). (O) Post hoc immunostaining of (N) showing elongated mRFP$^+$Tbr1$^+$Sp8$^-$ cells (arrows).
(P–R) Immunostaining (P) and quantification of density (Q) and number/section (R) of human PL DCX$^+$ cells with a single process.
*p < 0.05, **p < 0.01, ***p < 0.001, one-way ANOVA Holm-Sidak's test. Data are mean ± SEM. Scale bars: 100 μm in (E); 50 μm in (A); 20 μm in (B), (G)–(I), and (N)–(P); 2 μm in (C, top left) and (D, top); and 500 nm in (C, bottom and right) and (D, bottom). See also Figure S11 and Video S3.

Please cite this article in press as: Alderman et al., Delayed maturation and migration of excitatory neurons in the juvenile mouse paralaminar amygdala, Neuron (2023), https://doi.org/10.1016/j.neuron.2023.11.010

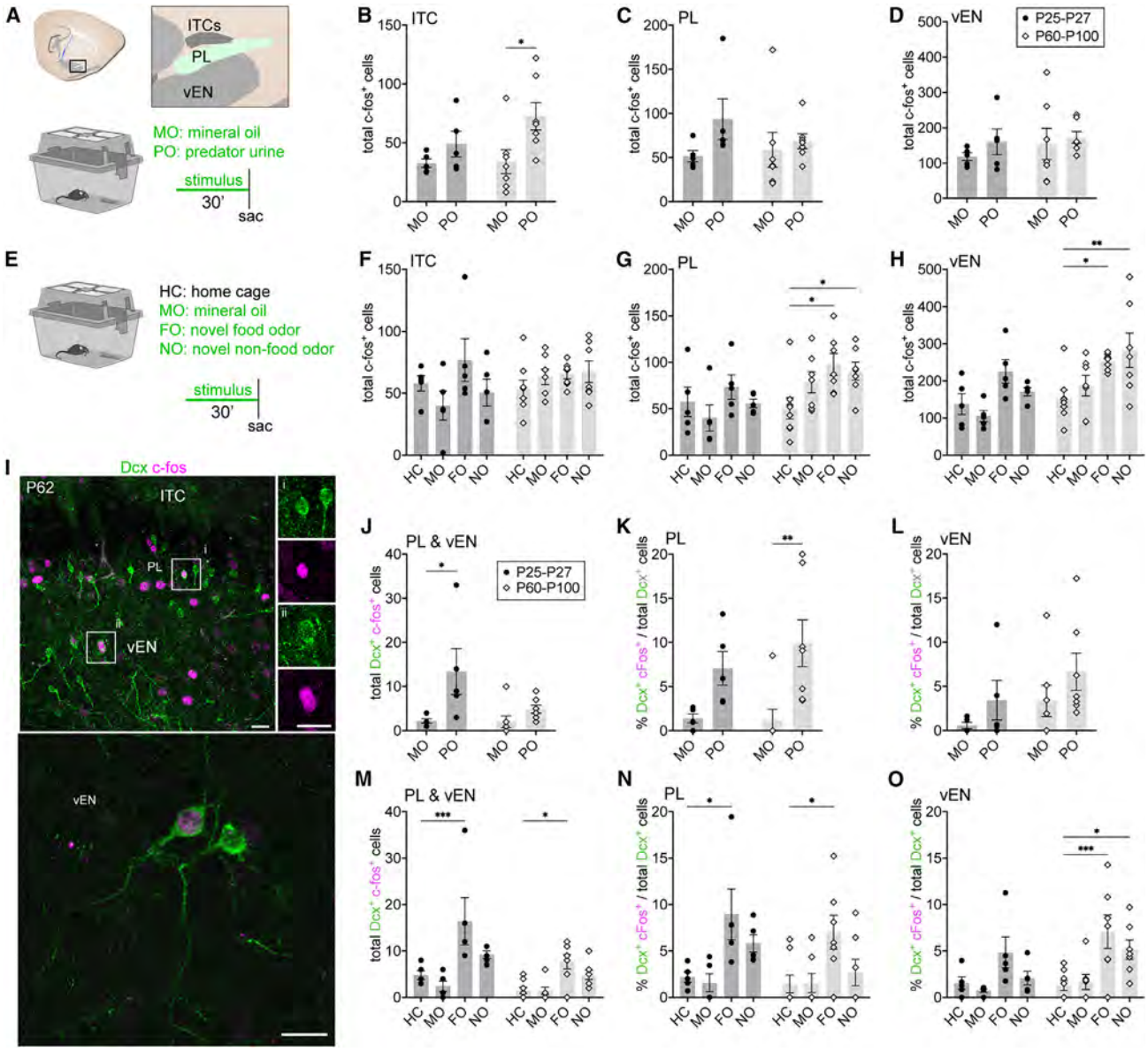

Figure 8. Mouse PL, ITC, and vEN neuron responses to olfactory stimuli in juveniles and adults

(A–D) Experimental scheme and quantification of c-Fos$^+$ cells in the ITC (B), PL (C), and vEN (D).

(E–H) Experimental scheme and quantification of total c-Fos$^+$ cells in the ITC (F), PL (G), and vEN (H).

(I) Immunostaining of Dcx$^+$c-Fos$^+$ cells post-FO in the adult PL and vEN (insets i and ii) and with complex morphology in the vEN (bottom).

(J–O) (J and M) Quantification of total Dcx$^+$c-Fos$^+$ cells and (K, L, N, and O) percentage of Dcx$^+$ cells that were c-Fos$^+$.

*p < 0.05, **p < 0.01, ***p < 0.001, two-way ANOVA with Holm-Sidak's test. Data are mean ± SEM. Scale bars: 20 μm in (I).

- Marker co-expression quantification
- Cell morphology reconstructions and mapping
- Olfactory stimulus exposure
- Transmission electron microscopy and immunogold labeling
- Electrophysiology
- iDISCO staining and light sheet microscopy
- Time-lapse microscopy and migratory neuron tracking
- Human tissue immunofluorescence
- Single cell dissociation and RNA-sequencing
- Single cell RNA sequencing analysis
- Open source gene expression analysis
- Statistical analysis

SUPPLEMENTAL INFORMATION

Supplemental information can be found online at https://doi.org/10.1016/j.neuron.2023.11.010.

ACKNOWLEDGMENTS

S.F.S., P.J.A., C.E.P., M.S., J.K.B., D.S., and J.G.C. acknowledge the National Institute of Mental Health (NIMH) (R21MH125367 and R01MH128745). J.M.G.-V. was supported by the Valencian Council for Innovation Universities, Science, and Digital Society (PROMETEO/2019/075) and V.H.-P. by the Spanish Ministry of Science, Innovation, and Universities (PCI2018-093062). We thank Drs. Julia Kofler and Clayton Wiley, University of Pittsburgh, and Eric Huang, University of California, San Francisco, for human samples and the Duke Neurotransgenic Core Facility and Ute Hochgeschwender for the Dcx-CreER™ line. We thank Sorrells and Corbin lab members for feedback throughout the course of the project, Dr. Marcos Assis Nascimento for transcriptomic analysis consultations, and Dr. Arturo Alvarez-Buylla and Quetzal Flores-Ramirez for early discussions.

AUTHOR CONTRIBUTIONS

P.J.A. and S.F.S. initially conceptualized the study, conceived the experiments, and wrote the manuscript. P.J.A. performed mouse immunostainings, confocal microscopy, stereology, birth dating, time-lapse imaging, cell mapping, and odorant exposures, advised by S.F.S. D.S. performed mouse light-sheet imaging and with V.A.B. performed embryonic lineage tracing, advised by J.G.C. D.S. performed mouse electrophysiological recordings, advised by S.V. and J.G.C. L.I.T.-S. and V.H.-P. performed transmission electron microscopy and analysis, advised by J.M.G.-V. S.W.B., M.S., and S.F.S. processed, stained, and analyzed human samples. P.J.A. and M.S. performed mouse embryology experiments and with C.E.P. and A.M. quantified co-localized cells, advised by S.F.S. C.T.K. contributed Dcx-CreER™ mice and their preliminary characterization. P.J.A. and J.K.B. performed single-cell RNA sequencing, analyzed by J.K.B. and S.F.S. D.S., C.E.P., V.H.-P., and J.G.C. provided manuscript draft revisions. Funding for the study was obtained by J.G.C. and S.F.S. S.F.S. initiated and directed the study and wrote the manuscript with input from all authors.

DECLARATION OF INTERESTS

The authors declare no competing interests.

Received: November 22, 2022
Revised: May 5, 2023
Accepted: November 9, 2023
Published: December 11, 2023

REFERENCES

1. Jin, J., Zelano, C., Gottfried, J.A., and Mohanty, A. (2015). Human amygdala represents the complete spectrum of subjective valence. J. Neurosci. *35*, 15145–15156.
2. Janak, P.H., and Tye, K.M. (2015). From circuits to behaviour in the amygdala. Nature *517*, 284–292.
3. Scherf, K.S., Smyth, J.M., and Delgado, M.R. (2013). The amygdala: an agent of change in adolescent neural networks. Horm. Behav. *64*, 298–313.
4. Nabel, E.M., Garkun, Y., Koike, H., Sadahiro, M., Liang, A., Norman, K.J., Taccheri, G., Demars, M.P., Im, S., Caro, K., et al. (2020). Adolescent frontal top-down neurons receive heightened local drive to establish adult attentional behavior in mice. Nat. Commun. *11*, 3983.
5. Ferrara, N.C., Trask, S., and Rosenkranz, J.A. (2021). Maturation of amygdala inputs regulate shifts in social and fear behaviors: A substrate for developmental effects of stress. Neurosci. Biobehav. Rev. *125*, 11–25.
6. Sorrells, S.F., Paredes, M.F., Velmeshev, D., Herranz-Pérez, V., Sandoval, K., Mayer, S., Chang, E.F., Insausti, R., Kriegstein, A.R., Rubenstein, J.L., et al. (2019). Immature excitatory neurons develop during adolescence in the human amygdala. Nat. Commun. *10*, 2748.
7. Avino, T.A., Barger, N., Vargas, M.V., Carlson, E.L., Amaral, D.G., Bauman, M.D., and Schumann, C.M. (2018). Neuron numbers increase in the human amygdala from birth to adulthood, but not in autism. Proc. Natl. Acad. Sci. USA *115*, 3710–3715.
8. Page, C.E., Biagiotti, S.W., Alderman, P.J., and Sorrells, S.F. (2022). Immature excitatory neurons in the amygdala come of age during puberty. Dev. Cogn. Neurosci. *56*, 101133.
9. Ostby, Y., Tamnes, C.K., Fjell, A.M., Westlye, L.T., Due-Tønnessen, P., and Walhovd, K.B. (2009). Heterogeneity in subcortical brain development: A structural magnetic resonance imaging study of brain maturation from 8 to 30 years. J. Neurosci. *29*, 11772–11782.
10. Uematsu, A., Matsui, M., Tanaka, C., Takahashi, T., Noguchi, K., Suzuki, M., and Nishijo, H. (2012). Developmental trajectories of amygdala and hippocampus from infancy to early adulthood in healthy individuals. PLoS One *7*, e46970.
11. Martí-Mengual, U., Varea, E., Crespo, C., Blasco-Ibáñez, J.M., and Nacher, J. (2013). Cells expressing markers of immature neurons in the amygdala of adult humans. Eur. J. Neurosci. *37*, 10–22.
12. deCampo, D.M., and Fudge, J.L. (2012). Where and what is the paralaminar nucleus? A review on a unique and frequently overlooked area of the primate amygdala. Neurosci. Biobehav. Rev. *36*, 520–535.
13. La Rosa, C., Ghibaudi, M., and Bonfanti, L. (2019). Newly generated and non-newly generated "immature" neurons in the mammalian brain: A possible reservoir of young cells to prevent brain aging and disease? J. Clin. Med. *8*, 685.
14. Palazzo, O., La Rosa, C., Piumatti, M., and Bonfanti, L. (2018). Do large brains of long-living mammals prefer non-newly generated, immature neurons? Neural Regen. Res. *13*, 633–634.
15. Benedetti, B., Dannehl, D., König, R., Coviello, S., Kreutzer, C., Zaunmair, P., Jakubecova, D., Weiger, T.M., Aigner, L., Nacher, J., et al. (2020). Functional integration of neuronal precursors in the adult murine piriform cortex. Cereb. Cortex *30*, 1499–1515.
16. Benedetti, B., and Couillard-Despres, S. (2022). Why would the brain need dormant neuronal precursors? Front. Neurosci. *16*, 877167.
17. Sanides, F. (1957). Histological structure of the amygdaloid nucleus region. I. Cytology and involution of amygdaleum profundum. J. Hirnforsch. *3*, 56–77.
18. Li, Y.-N., Hu, D.-D., Cai, X.-L., Wang, Y., Yang, C., Jiang, J., Zhang, Q.-L., Tu, T., Wang, X.-S., Wang, H., et al. (2023). Doublecortin-expressing neurons in human cerebral cortex Layer II and amygdala from infancy to 100 years old. Mol. Neurobiol. *60*, 3464–3485.
19. Zhang, X.M., Cai, Y., Chu, Y., Chen, E.Y., Feng, J.C., Luo, X.G., Xiong, K., Struble, R.G., Clough, R.W., Patrylo, P.R., et al. (2009). Doublecortin-expressing cells persist in the associate cerebral cortex and amygdala in aged nonhuman primates. Front. Neuroanat. *3*, 17.
20. Chareyron, L.J., Lavenex, P.B., Amaral, D.G., and Lavenex, P. (2012). Postnatal development of the amygdala: A stereological study in macaque monkeys. J. Comp. Neurol. *520*, 1965–1984.
21. Chareyron, L.J., Amaral, D.G., and Lavenex, P. (2016). Selective lesion of the hippocampus increases the differentiation of immature neurons in the monkey amygdala. Proc. Natl. Acad. Sci. USA *113*, 14420–14425.
22. Fudge, J.L. (2004). Bcl-2 immunoreactive neurons are differentially distributed in subregions of the amygdala and hippocampus of the adult macaque. Neuroscience *127*, 539–556.
23. McHale-Matthews, A.C., DeCampo, D.M., Love, T., Cameron, J.L., and Fudge, J.L. (2023). Immature neurons in the primate amygdala: changes with early development and disrupted early environment. Dev. Cogn. Neurosci. *61*, 101248.
24. Chareyron, L.J., Banta Lavenex, P., Amaral, D.G., and Lavenex, P. (2021). Life and death of immature neurons in the juvenile and adult primate amygdala. Int. J. Mol. Sci. *22*, 6691.

25. García-Amado, M., and Prensa, L. (2012). Stereological analysis of neuron, glial and endothelial cell numbers in the human amygdaloid complex. PLoS One *7*, e38692.

26. Ghibaudi, M., and Bonfanti, L. (2022). How widespread are the "young" neurons of the mammalian brain? Front. Neurosci. *16*, 918616.

27. Piumatti, M., Palazzo, O., La Rosa, C., Crociara, P., Parolisi, R., Luzzati, F., Lévy, F., and Bonfanti, L. (2018). Non-newly generated, "immature" neurons in the sheep brain are not restricted to cerebral cortex. J. Neurosci. *38*, 826–842.

28. Sah, P., Faber, E.S.L., Lopez De Armentia, M., and Power, J. (2003). The amygdaloid complex: anatomy and physiology. Physiol. Rev. *83*, 803–834.

29. Luzzati, F., Bonfanti, L., Fasolo, A., and Peretto, P. (2009). DCX and PSA-NCAM expression identifies a population of neurons preferentially distributed in associative areas of different pallial derivatives and vertebrate species. Cereb. Cortex *19*, 1028–1041.

30. Caroline Crosby, E., and Humphrey, T. (1939). Studies of the vertebrate telencephalon. I. The nuclear configuration of the olfactory and accessory olfactory formations and of the nucleus olfactorius anterior of certain reptiles, birds, and mammals. J. Comp. Neurol. *71*, 121–213.

31. Ai, J.-Q., Luo, R., Tu, T., Yang, C., Jiang, J., Zhang, B., Bi, R., Tu, E., Yao, Y.-G., and Yan, X.-X. (2021). Doublecortin-expressing neurons in Chinese tree shrew forebrain exhibit mixed rodent and primate-like topographic characteristics. Front. Neuroanat. *15*, 727883.

32. Bernier, P.J., Bedard, A., Vinet, J., Levesque, M., and Parent, A. (2002). Newly generated neurons in the amygdala and adjoining cortex of adult primates. Proc. Natl. Acad. Sci. USA *99*, 11464–11469.

33. Marlatt, M.W., Philippens, I., Manders, E., Czéh, B., Joels, M., Krugers, H., and Lucassen, P.J. (2011). Distinct structural plasticity in the hippocampus and amygdala of the middle-aged common marmoset (Callithrix jacchus). Exp. Neurol. *230*, 291–301.

34. Roeder, S.S., Burkardt, P., Rost, F., Rode, J., Brusch, L., Coras, R., Englund, E., Håkansson, K., Possnert, G., Salehpour, M., et al. (2022). Evidence for postnatal neurogenesis in the human amygdala. Commun. Biol. *5*, 366.

35. Ulfig, N., Setzer, M., and Bohl, J. (2003). Ontogeny of the human amygdala. Ann. N. Y. Acad. Sci. *985*, 22–33.

36. Jhaveri, D.J., Tedoldi, A., Hunt, S., Sullivan, R., Watts, N.R., Power, J.M., Bartlett, P.F., and Sah, P. (2018). Evidence for newly generated interneurons in the basolateral amygdala of adult mice. Mol. Psychiatry *23*, 521–532.

37. Shapiro, L.A., Ng, K., Zhou, Q.-Y., and Ribak, C.E. (2009). Subventricular zone-derived, newly generated neurons populate several olfactory and limbic forebrain regions. Epilepsy Behav. *14* (*Suppl 1*), 74–80.

38. Rakic, P. (2002). Neurogenesis in adult primate neocortex: an evaluation of the evidence. Nat. Rev. Neurosci. *3*, 65–71.

39. Boulanger, J.J., and Messier, C. (2017). Doublecortin in oligodendrocyte precursor cells in the adult mouse brain. Front. Neurosci. *11*, 143.

40. Saul, M.L., Helmreich, D.L., Rehman, S., and Fudge, J.L. (2015). Proliferating cells in the adolescent rat amygdala: characterization and response to stress. Neuroscience *311*, 105–117.

41. Ehninger, D., Wang, L.-P., Klempin, F., Römer, B., Kettenmann, H., and Kempermann, G. (2011). Enriched environment and physical activity reduce microglia and influence the fate of NG2 cells in the amygdala of adult mice. Cell Tissue Res. *345*, 69–86.

42. Takemura, N.U. (2005). Evidence for neurogenesis within the white matter beneath the temporal neocortex of the adult rat brain. Neuroscience *134*, 121–132.

43. Paredes, M.F., Sorrells, S.F., Cebrian-Silla, A., Sandoval, K., Qi, D., Kelley, K.W., James, D., Mayer, S., Chang, J., Auguste, K.I., et al. (2018). Does adult neurogenesis persist in the human hippocampus? Cell Stem Cell *23*, 780–781.

44. Lois, C., and Alvarez-Buylla, A. (1994). Long-distance neuronal migration in the adult mammalian brain. Science *264*, 1145–1148.

45. Zhao, C., Teng, E.M., Summers, R.G., Jr., Ming, G.-L., and Gage, F.H. (2006). Distinct morphological stages of dentate granule neuron maturation in the adult mouse hippocampus. J. Neurosci. *26*, 3–11.

46. Smith, J.B., Alloway, K.D., Hof, P.R., Orman, R., Reser, D.H., Watakabe, A., and Watson, G.D.R. (2019). The relationship between the claustrum and endopiriform nucleus: A perspective towards consensus on cross-species homology. J. Comp. Neurol. *527*, 476–499.

47. Kuerbitz, J., Arnett, M., Ehrman, S., Williams, M.T., Vorhees, C.V., Fisher, S.E., Garratt, A.N., Muglia, L.J., Waclaw, R.R., and Campbell, K. (2018). Loss of intercalated cells (ITCs) in the mouse amygdala of *Tshz1* mutants correlates with fear, depression, and social interaction phenotypes. J. Neurosci. *38*, 1160–1177.

48. Kuerbitz, J., Madhavan, M., Ehrman, L.A., Kohli, V., Waclaw, R.R., and Campbell, K. (2021). Temporally distinct roles for the zinc finger transcription factor Sp8 in the generation and migration of dorsal lateral ganglionic eminence (dLGE)-derived neuronal subtypes in the mouse. Cereb. Cortex *31*, 1744–1762.

49. Hagihara, K.M., Bukalo, O., Zeller, M., Aksoy-Aksel, A., Karalis, N., Limoges, A., Rigg, T., Campbell, T., Mendez, A., Weinholtz, C., et al. (2021). Intercalated amygdala clusters orchestrate a switch in fear state. Nature *594*, 403–407.

50. Workman, A.D., Charvet, C.J., Clancy, B., Darlington, R.B., and Finlay, B.L. (2013). Modeling transformations of neurodevelopmental sequences across mammalian species. J. Neurosci. *33*, 7368–7383.

51. Dutta, S., and Sengupta, P. (2016). Men and mice: relating their ages. Life Sci. *152*, 244–248.

52. Waclaw, R.R., Ehrman, L.A., Pierani, A., and Campbell, K. (2010). Developmental origin of the neuronal subtypes that comprise the amygdalar fear circuit in the mouse. J. Neurosci. *30*, 6944–6953.

53. Li, J., Wang, C., Zhang, Z., Wen, Y., An, L., Liang, Q., Xu, Z., Wei, S., Li, W., Guo, T., et al. (2018). Transcription factors Sp8 and Sp9 coordinately regulate olfactory bulb interneuron development. Cereb. Cortex *28*, 3278–3294.

54. Bruguier, H., Suarez, R., Manger, P., Hoerder-Suabedissen, A., Shelton, A.M., Oliver, D.K., Packer, A.M., Ferran, J.L., García-Moreno, F., Puelles, L., and Molnár, Z. (2020). In search of common developmental and evolutionary origin of the claustrum and subplate. J. Comp. Neurol. *528*, 2956–2977.

55. Puelles, L., Kuwana, E., Puelles, E., Bulfone, A., Shimamura, K., Keleher, J., Smiga, S., and Rubenstein, J.L. (2000). Pallial and subpallial derivatives in the embryonic chick and mouse telencephalon, traced by the expression of the genes Dlx-2, Emx-1, Nkx-2.1, Pax-6, and Tbr-1. J. Comp. Neurol. *424*, 409–438.

56. Renier, N., Wu, Z., Simon, D.J., Yang, J., Ariel, P., and Tessier-Lavigne, M. (2014). iDISCO: a simple, rapid method to immunolabel large tissue samples for volume imaging. Cell *159*, 896–910.

57. Wang, W., Wang, M., Yang, M., Zeng, B., Qiu, W., Ma, Q., Jing, X., Zhang, Q., Wang, B., Yin, C., et al. (2022). Transcriptome dynamics of hippocampal neurogenesis in macaques across the lifespan and aged humans. Cell Res. *32*, 729–743.

58. Zhang, M., Pan, X., Jung, W., Halpern, A., Eichhorn, S.W., Lei, Z., Cohen, L., Smith, K.A., Tasic, B., Yao, Z., et al. (2023). A molecularly defined and spatially resolved cell atlas of the whole mouse brain. Preprint at bioRxiv.

59. Yu, B., Zhang, Q., Lin, L., Zhou, X., Ma, W., Wen, S., Li, C., Wang, W., Wu, Q., Wang, X., and Li, X.M. (2023). Molecular and cellular evolution of the amygdala across species analyzed by single-nucleus transcriptome profiling. Cell Discov. *9*, 19.

60. Englund, C., Fink, A., Lau, C., Pham, D., Daza, R.A.M., Bulfone, A., Kowalczyk, T., and Hevner, R.F. (2005). Pax6, Tbr2, and Tbr1 are expressed sequentially by radial glia, intermediate progenitor cells, and postmitotic neurons in developing neocortex. J. Neurosci. *25*, 247–251.

61. Iwano, T., Masuda, A., Kiyonari, H., Enomoto, H., and Matsuzaki, F. (2012). Prox1 postmitotically defines dentate gyrus cells by specifying granule cell identity over CA3 pyramidal cell fate in the hippocampus. Development *139*, 3051–3062.

62. Franjic, D., Skarica, M., Ma, S., Arellano, J.I., Tebbenkamp, A.T.N., Choi, J., Xu, C., Li, Q., Morozov, Y.M., Andrijevic, D., et al. (2022). Transcriptomic taxonomy and neurogenic trajectories of adult human, macaque, and pig hippocampal and entorhinal cells. Neuron *110*, 452–469.e14.

63. Porter, A.G., and Jänicke, R.U. (1999). Emerging roles of caspase-3 in apoptosis. Cell Death Differ. *6*, 99–104.

64. Wong, F.K., Bercsenyi, K., Sreenivasan, V., Portalés, A., Fernández-Otero, M., and Marín, O. (2018). Pyramidal cell regulation of interneuron survival sculpts cortical networks. Nature *557*, 668–673.

65. Southwell, D.G., Paredes, M.F., Galvao, R.P., Jones, D.L., Froemke, R.C., Sebe, J.Y., Alfaro-Cervello, C., Tang, Y., Garcia-Verdugo, J.M., Rubenstein, J.L., et al. (2012). Intrinsically determined cell death of developing cortical interneurons. Nature *491*, 109–113.

66. Ota, H., Hikita, T., Sawada, M., Nishioka, T., Matsumoto, M., Komura, M., Ohno, A., Kamiya, Y., Miyamoto, T., Asai, N., et al. (2014). Speed control for neuronal migration in the postnatal brain by Gmip-mediated local inactivation of RhoA. Nat. Commun. *5*, 4532.

67. Lim, L., Mi, D., Llorca, A., and Marín, O. (2018). Development and functional diversification of cortical interneurons. Neuron *100*, 294–313.

68. Hayashi, K., Kubo, K.-I., Kitazawa, A., and Nakajima, K. (2015). Cellular dynamics of neuronal migration in the hippocampus. Front. Neurosci. *9*, 135.

69. Kriegstein, A.R., and Noctor, S.C. (2004). Patterns of neuronal migration in the embryonic cortex. Trends Neurosci. *27*, 392–399.

70. Sugai, T., Yamamoto, R., Yoshimura, H., and Kato, N. (2012). Multimodal cross-talk of olfactory and gustatory information in the endopiriform nucleus in rats. Chem. Senses *37*, 681–688.

71. Ferrero, D.M., Lemon, J.K., Fluegge, D., Pashkovski, S.L., Korzan, W.J., Datta, S.R., Spehr, M., Fendt, M., and Liberles, S.D. (2011). Detection and avoidance of a carnivore odor by prey. Proc. Natl. Acad. Sci. USA *108*, 11235–11240.

72. Sorrells, S.F., Paredes, M.F., Zhang, Z., Kang, G., Pastor-Alonso, O., Biagiotti, S., Page, C.E., Sandoval, K., Knox, A., Connolly, A., et al. (2021). Positive controls in adults and children support that very few, if any, new neurons are born in the adult human hippocampus. J. Neurosci. *41*, 2554–2565.

73. Moreno-Jiménez, E.P., Terreros-Roncal, J., Flor-García, M., Rábano, A., and Llorens-Martín, M. (2021). Evidences for adult hippocampal neurogenesis in humans. J. Neurosci. *41*, 2541–2553.

74. Seri, B., García-Verdugo, J.M., McEwen, B.S., and Alvarez-Buylla, A. (2001). Astrocytes give rise to new neurons in the adult mammalian hippocampus. J. Neurosci. *21*, 7153–7160.

75. van Praag, H., Schinder, A.F., Christie, B.R., Toni, N., Palmer, T.D., and Gage, F.H. (2002). Functional neurogenesis in the adult hippocampus. Nature *415*, 1030–1034.

76. Rotheneichner, P., Belles, M., Benedetti, B., König, R., Dannehl, D., Kreutzer, C., Zaunmair, P., Engelhardt, M., Aigner, L., Nacher, J., and Couillard-Despres, S. (2018). Cellular plasticity in the adult murine piriform cortex: continuous maturation of dormant precursors into excitatory neurons. Cereb. Cortex *28*, 2610–2621.

77. Rubio, A., Belles, M., Belenguer, G., Vidueira, S., Fariñas, I., and Nacher, J. (2016). Characterization and isolation of immature neurons of the adult mouse piriform cortex. Dev. Neurobiol. *76*, 748–763.

78. Klempin, F., Kronenberg, G., Cheung, G., Kettenmann, H., and Kempermann, G. (2011). Properties of doublecortin-(DCX)-expressing cells in the piriform cortex compared to the neurogenic dentate gyrus of adult mice. PLoS ONE *6*, e25760.

79. Zhou, Y., Su, Y., Li, S., Kennedy, B.C., Zhang, D.Y., Bond, A.M., Sun, Y., Jacob, F., Lu, L., Hu, P., et al. (2022). Molecular landscapes of human hippocampal immature neurons across lifespan. Nature *607*, 527–533.

80. Moreno-Jiménez, E.P., Flor-García, M., Terreros-Roncal, J., Rábano, A., Cafini, F., Pallas-Bazarra, N., Ávila, J., and Llorens-Martín, M. (2019). Adult hippocampal neurogenesis is abundant in neurologically healthy subjects and drops sharply in patients with Alzheimer's disease. Nat. Med. *25*, 554–560.

81. Dennis, C.V., Suh, L.S., Rodriguez, M.L., Kril, J.J., and Sutherland, G.T. (2016). Human adult neurogenesis across the ages: an immunohistochemical study. Neuropathol. Appl. Neurobiol. *42*, 621–638.

82. Cipriani, S., Ferrer, I., Aronica, E., Kovacs, G.G., Verney, C., Nardelli, J., Khung, S., Delezoide, A.-L., Milenkovic, I., Rasika, S., et al. (2018). Hippocampal radial glial subtypes and their neurogenic potential in human fetuses and healthy and Alzheimer's disease adults. Cereb. Cortex *28*, 2458–2478.

83. Overstreet-Wadiche, L.S., Bensen, A.L., and Westbrook, G.L. (2006). Delayed development of adult-generated granule cells in dentate gyrus. J. Neurosci. *26*, 2326–2334.

84. Tozuka, Y., Fukuda, S., Namba, T., Seki, T., and Hisatsune, T. (2005). GABAergic excitation promotes neuronal differentiation in adult hippocampal progenitor cells. Neuron *47*, 803–815.

85. Ge, S., Goh, E.L.K., Sailor, K.A., Kitabatake, Y., Ming, G.-L., and Song, H. (2006). GABA regulates synaptic integration of newly generated neurons in the adult brain. Nature *439*, 589–593.

86. Vereczki, V.K., Müller, K., Krizsán, É., Máté, Z., Fekete, Z., Rovira-Esteban, L., Veres, J.M., Erdélyi, F., and Hájos, N. (2021). Total number and ratio of GABAergic neuron types in the mouse lateral and basal amygdala. J. Neurosci. *41*, 4575–4595.

87. Chawana, R., Patzke, N., Alagaili, A.N., Bennett, N.C., Mohammed, O.B., Kaswera-Kyamakya, C., Gilissen, E., Ihunwo, A.O., Pettigrew, J.D., and Manger, P.R. (2016). The distribution of Ki-67 and doublecortin immunopositive cells in the brains of three microchiropteran species, Hipposideros fuliginosus, Triaenops persicus, and Asellia tridens. Anat. Rec. (Hoboken) *299*, 1548–1560.

88. Doetsch, F., and Alvarez-Buylla, A. (1996). Network of tangential pathways for neuronal migration in adult mammalian brain. Proc. Natl. Acad. Sci. USA *93*, 14895–14900.

89. Bayer, S.A., Altman, J., Russo, R.J., Dai, X.F., and Simmons, J.A. (1991). Cell migration in the rat embryonic neocortex. J. Comp. Neurol. *307*, 499–516.

90. Carney, R.S.E., Alfonso, T.B., Cohen, D., Dai, H., Nery, S., Stoica, B., Slotkin, J., Bregman, B.S., Fishell, G., and Corbin, J.G. (2006). Cell migration along the lateral cortical stream to the developing basal telencephalic limbic system. J. Neurosci. *26*, 11562–11574.

91. Hirata, T., Li, P., Lanuza, G.M., Cocas, L.A., Huntsman, M.M., and Corbin, J.G. (2009). Identification of distinct telencephalic progenitor pools for neuronal diversity in the amygdala. Nat. Neurosci. *12*, 141–149.

92. Bonfanti, L., La Rosa, C., Ghibaudi, M., and Sherwood, C.C. (2023). Adult neurogenesis and "immature" neurons in mammals: an evolutionary trade-off in plasticity? Brain Struct. Funct. https://pubmed.ncbi.nlm.nih.gov/37833544/.

93. La Rosa, C., Parolisi, R., and Bonfanti, L. (2020). Brain structural plasticity: from adult neurogenesis to immature neurons. Front. Neurosci. *14*, 75.

94. Anacker, C., and Hen, R. (2017). Adult hippocampal neurogenesis and cognitive flexibility - linking memory and mood. Nat. Rev. Neurosci. *18*, 335–346.

95. Sorrells, S.F., Paredes, M.F., Cebrian-Silla, A., Sandoval, K., Qi, D., Kelley, K.W., James, D., Mayer, S., Chang, J., Auguste, K.I., et al. (2018). Human hippocampal neurogenesis drops sharply in children to undetectable levels in adults. Nature *555*, 377–381.

96. Paredes, M.F., Sorrells, S.F., Garcia-Verdugo, J.M., and Alvarez-Buylla, A. (2016). Brain size and limits to adult neurogenesis. J. Comp. Neurol. *524*, 646–664.

97. Weinandy, F., Ninkovic, J., and Götz, M. (2011). Restrictions in time and space–new insights into generation of specific neuronal subtypes in the adult mammalian brain. Eur. J. Neurosci. *33*, 1045–1054.

98. Snyder, J.S. (2019). Recalibrating the relevance of adult neurogenesis. Trends Neurosci. *42*, 164–178.

99. de Campo, D.M., Cameron, J.L., Miano, J.M., Lewis, D.A., Mirnics, K., and Fudge, J.L. (2017). Maternal deprivation alters expression of neural maturation gene tbr1 in the amygdala paralaminar nucleus in infant female macaques. Dev. Psychobiol. *59*, 235–249.

100. Kessler, R.C., Amminger, G.P., Aguilar-Gaxiola, S., Alonso, J., Lee, S., and Ustün, T.B. (2007). Age of onset of mental disorders: a review of recent literature. Curr. Opin. Psychiatry *20*, 359–364.

101. Campbell, C.E., Mezher, A.F., Eckel, S.P., Tyszka, J.M., Pauli, W.M., Nagel, B.J., and Herting, M.M. (2021). Restructuring of amygdala subregion apportion across adolescence. Dev. Cogn. Neurosci. *48*, 100883.

102. Villard, J., Bennett, J.L., Bliss-Moreau, E., Capitanio, J.P., Fox, N.A., Amaral, D.G., and Lavenex, P. (2021). Structural differences in the hippocampus and amygdala of behaviorally inhibited macaque monkeys. Hippocampus *31*, 858–868.

103. VanTieghem, M., Korom, M., Flannery, J., Choy, T., Caldera, C., Humphreys, K.L., Gabard-Durnam, L., Goff, B., Gee, D.G., Telzer, E.H., et al. (2021). Longitudinal changes in amygdala, hippocampus and cortisol development following early caregiving adversity. Dev. Cogn. Neurosci. *48*, 100916.

104. Hessl, D., Libero, L., Schneider, A., Kerns, C., Winder-Patel, B., Heath, B., Lee, J., Coleman, C., Sharma, N., Solomon, M., et al. (2021). Fear potentiated startle in children with autism spectrum disorder: association with anxiety symptoms and amygdala volume. Autism Res. *14*, 450–463.

105. Schumann, C.M., Bauman, M.D., and Amaral, D.G. (2011). Abnormal structure or function of the amygdala is a common component of neurodevelopmental disorders. Neuropsychologia *49*, 745–759.

106. Liu, J.Y.W., Matarin, M., Reeves, C., McEvoy, A.W., Miserocchi, A., Thompson, P., Sisodiya, S.M., and Thom, M. (2018). Doublecortin-expressing cell types in temporal lobe epilepsy. Acta Neuropathol. Commun. *6*, 60.

107. Maheu, M.E., Davoli, M.A., Turecki, G., and Mechawar, N. (2013). Amygdalar expression of proteins associated with neuroplasticity in major depression and suicide. J. Psychiatr. Res. *47*, 384–390.

108. Hayashi, S., and McMahon, A.P. (2002). Efficient recombination in diverse tissues by a tamoxifen-inducible form of Cre: a tool for temporally regulated gene activation/inactivation in the mouse. Dev. Biol. *244*, 305–318.

109. Arenkiel, B.R., Hasegawa, H., Yi, J.J., Larsen, R.S., Wallace, M.L., Philpot, B.D., Wang, F., and Ehlers, M.D. (2011). Activity-induced remodeling of olfactory bulb microcircuits revealed by monosynaptic tracing. PLoS One *6*, e29423.

110. Sirerol-Piquer, M.S., Cebrián-Silla, A., Alfaro-Cervelló, C., Gomez-Pinedo, U., Soriano-Navarro, M., and Verdugo, J.-M.G. (2012). GFP immunogold staining, from light to electron microscopy, in mammalian cells. Micron *43*, 589–599.

111. Stuart, T., Butler, A., Hoffman, P., Hafemeister, C., Papalexi, E., Mauck, W.M., 3rd, Hao, Y., Stoeckius, M., Smibert, P., and Satija, R. (2019). Comprehensive integration of single-cell data. Cell *177*, 1888–1902.e21.

112. Lein, E.S., Hawrylycz, M.J., Ao, N., Ayres, M., Bensinger, A., Bernard, A., Boe, A.F., Boguski, M.S., Brockway, K.S., Byrnes, E.J., et al. (2007). Genome-wide atlas of gene expression in the adult mouse brain. Nature *445*, 168–176.

Please cite this article in press as: Alderman et al., Delayed maturation and migration of excitatory neurons in the juvenile mouse paralaminar amygdala, Neuron (2023), https://doi.org/10.1016/j.neuron.2023.11.010

STAR★METHODS

KEY RESOURCES TABLE

REAGENT or RESOURCE	SOURCE	IDENTIFIER
Antibodies		
Mouse anti-APC (1:000)	Millipore-Sigma	Cat. # OP80; lot # 3307277; RRID:AB_2057371
Rabbit anti-Arc (1:500)	ThermoFisher	Cat. # 16290-1-AP; lot # 00094124; RRID:AB_2151832
Rat anti-BrdU (1:200)	Abcam	Cat. # AB6326; lot # GR3365969-10; RRID:AB_305426
Rabbit anti-c-Fos (1:500)	Encor	Cat. # RPCA-c-FOS; lot # 1732041422; RRID:AB_2572236
Rabbit anti-Cleaved Caspase-3 (1:500)	Cell Signal	Cat. # 9664S; lot # 22; RRID:AB_2070042
Rabbit anti-CoupTFII (1:500)	Abcam	Cat. # AB211777; lot # GR3396420-9; RRID:AB_2895604
Mouse anti-CoupTFII (1:250 IHC 1:100 EM)	R&D Systems	Cat. # PP-H7147-00; lot # A-2; RRID:AB_2155627
Rat anti-Ctip2 (1:200)	Abcam	Cat. # AB18465; lot # gr243609-4; RRID:AB_2064130
Rabbit anti-Dcx (1:500 IHC 1:100 EM)	Cell Signal	Cat. # 4604; lot # 6, 7; RRID:AB_561007
Guinea pig anti-Dcx (1:500)	EMD Millipore	Cat. # AB2253; lot # 3847922, 3777998, 3601335; RRID:AB_1586992
Rabbit anti-Egr1 (1:500)	ThermoFisher	Cat. # MA515008; lot # YB3846072; RRID:AB_10977090
Rabbit anti-FoxP2 (1:500)	Atlas Antibodies	Cat. # hpa000382; lot # B115858; RRID:AB_1078908
Goat anti-FoxP2 (1:500)	Santa Cruz Biotechnology	Cat. # 517261; lot # G2216; RRID:AB_2721204
Rabbit anti-GFAP (1:500)	EMD Millipore	Cat. # Z0334; lot # 3194598; RRID:AB_10013382
Rabbit anti-Ki67	Abcam	Cat. # AB15580; lot # 1012330-1; RRID:AB_443209
Mouse anti-Ki67	BD Bioscience	Cat. # 556003; lot # 1032658; RRID:AB_396287
Rat anti-Mcherry (tdTomato) 1:200	Invitrogen	Cat. # M11217; lot # WI334529, XC345714; RRID:AB_2536611
Chicken anti-NeuN (1:200)	EMD Millipore	Cat. # ABN91; lot # 3788621, 3788621; RRID:AB_11205760
Rabbit anti-Olig2 (1:500)	EMD Millipore	Cat. # AB9610; lot # 3755328; RRID:AB_570666
Mouse anti-Olig2 (1:1000)	EMD Millipore	Cat. # MABN50; lot # 3897261; RRID:AB_10807410
Rabbit anti-Pax6 (1:500)	Bio-Legend	Cat. # 901301; lot # B201255; RRID:AB_2565003
Rabbit anti-pH3 (1:500)	Fisher	Cat. # PA5-17869; lot # XL3790136; RRID:AB_10984484
Goat anti-Prox1 (1:200)	R&D Systems	Cat. # AF2727; lot # VIY0521041; RRID:AB_2170716
Mouse anti-Psa-Ncam (1:1000)	EMD Millipore	Cat. # MAB5324; lot # 3607061; RRID:AB_95211

(*Continued on next page*)

Please cite this article in press as: Alderman et al., Delayed maturation and migration of excitatory neurons in the juvenile mouse paralaminar amygdala, Neuron (2023), https://doi.org/10.1016/j.neuron.2023.11.010

Continued

REAGENT or RESOURCE	SOURCE	IDENTIFIER
Rabbit anti-SatB2 (1:500)	Abcam	Cat. # AB34735; lot # GR3354380-1; RRID:AB_2301417
Goat anti-Sp8 (1:500)	Santa Cruz Biotechnology	Cat. # sc-104661, lot # G0516; RRID:AB_2194626
Chicken anti-Tbr1 (1:500 IHC 1:100 EM)	EMD Millipore	Cat. # AB2261; lot # 3598056, 3105253, 3811721; RRID:AB_10615497
Rabbit anti-Tbr1 (1:500)	EMD Millipore	Cat. # AB10554; lot # 3598056, 3105253, 3811721; RRID:AB_10806888
Rabbit anti-Tbr2 (1:500)	Abcam	Cat. # AB216870; lot # GR3377770-4; RRID:AB_2943124
Alexa Fluor 488 Donkey anti-Rabbit IgG (H+L) (1:2000)	Invitrogen	Cat. # A32790; lot # TI271741; RRID:AB_2762833
Alexa Fluor 555 Donkey anti-Rabbit IgG (H+L) (1:2000)	Invitrogen	Cat. # A32794; lot # WG322207; RRID:AB_2762834
Donkey anti-Rabbit IgG (H+L) Highly Cross-Adsorbed Secondary Antibody, Alexa Fluor Plus 647 (1:2000)	Invitrogen	Cat. # A32795; lot # UG289708; RRID:AB_2762835
Goat anti-Rabbit IgG (H+L) Cross-Adsorbed Secondary Antibody, Alexa Fluor 647 (1:2000)	Invitrogen	Cat. # A21244; lot # 1463166; RRID:AB_2535812
Goat anti-Chicken IgY (H+L) Cross-Adsorbed Secondary Antibody, Alexa Fluor Plus 488 (1:2000)	Invitrogen	Cat. # A32931; lot # TI271747; RRID:AB_2762843
Alexa Fluor 488 AffiniPure Donkey Anti-Chicken IgY (IgG) (H+L) (1:2000)	Jackson ImmunoResearch	Cat. # 703-545-155; lot # 146581; RRID:AB_2340375
Alexa Fluor Cy3 AffiniPure Donkey Anti-Chicken IgY (IgG) (H+L) (1:2000)	Jackson ImmunoResearch	Cat. # 703-165-155; lot # 144929; RRID:AB_2340363
Alexa Fluor 647 AffiniPure Donkey Anti-Chicken IgY (IgG) (H+L) (1:2000)	Jackson ImmunoResearch	Cat. # 703-605-155; lot # 153969; RRID:AB_2340379
Alexa Fluor 488 AffiniPure Goat Anti-Rat IgG (H+L) (1:2000)	Jackson ImmunoResearch	Cat. # 112-545-167; lot # 148029; RRID:AB_2338362
Cy3 AffiniPure Donkey Anti-Rat IgG (H+L) (1:2000)	Jackson ImmunoResearch	Cat. # 712-165-153; lot # 156617; RRID:AB_2340667
Alexa Fluor 647 AffiniPure Donkey Anti-Rat IgG (H+L) (1:2000)	Jackson ImmunoResearch	Cat. # 712-605-153; lot # 154486; RRID:AB_2340694
Alexa Fluor 555 Goat anti-Guinea Pig IgG (H+L) (1:2000)	Invitrogen	Cat. # A21435; lot # 2076358; RRID:AB_2535856
Alexa Fluor 647 AffiniPure Donkey Anti-Guinea Pig IgG (H+L) (1:2000)	Jackson ImmunoResearch	Cat. # 706-605-148; lot # 149191; RRID:AB_2340476
Goat anti-Guinea Pig IgG (H+L) Highly Cross-Adsorbed Secondary Antibody, Alexa Fluor 647 (1:2000)	Invitrogen	Cat. # A21450; lot # 2110845; RRID:AB_141882
Alexa Fluor 488 AffiniPure Donkey Anti-Goat IgG (H+L) (1:2000)	Jackson ImmunoResearch	Cat. # 705-545-003; lot # 148783; RRID:AB_2340428
Alexa Fluor 488 AffiniPure Donkey Anti-Mouse IgG (H+L) (1:2000)	Invitrogen	Cat. # A32766; lot # TI271738; RRID:AB_2762823
Alexa Fluor 488 AffiniPure Goat Anti-Mouse IgM (H+L) (1:2000)	Invitrogen	Cat. # A21042; lot # 2079371; RRID:AB_2535711
Alexa Fluor 555 AffiniPure Donkey Anti-Mouse IgG (H+L) (1:2000)	Invitrogen	Cat. # A32773; lot # TI271028; RRID:AB_2762848
Alexa Fluor 555 AffiniPure Goat Anti-Mouse IgM (H+L) (1:2000)	Invitrogen	Cat. # A21426; lot # 2001027; RRID:AB_2535847

(*Continued on next page*)

Please cite this article in press as: Alderman et al., Delayed maturation and migration of excitatory neurons in the juvenile mouse paralaminar amygdala, Neuron (2023), https://doi.org/10.1016/j.neuron.2023.11.010

Continued

REAGENT or RESOURCE	SOURCE	IDENTIFIER
Donkey anti-Mouse IgG (H+L) Highly Cross-Adsorbed Secondary Antibody, Alexa Fluor Plus 647 (1:2000)	Invitrogen	Cat. # A32787; lot # 2001027; RRID:AB_2762830
Alexa Fluor 647 AffiniPure Goat Anti-Mouse IgM (H+L) (1:2000)	Invitrogen	Cat. # A21238; lot # 2112240; RRID:AB_2535807
Chemicals, peptides, and recombinant proteins		
Acetophenone	Sigma-Aldrich	Cat. # A10701
Adeonsine 5'-triphosphate magnesium salt (Mg-ATP)	Sigma	Cat. # A9187
Basal Medium Eagle (BME)	Thermofisher	Cat. # 21010046
Biotin-SP-AffiniPure Donkey Anti-Goat IgG (H+L) (1:500)	Jackson ImmunoResearch	Cat. # NC9494985
Biotin-SP-AffiniPure Goat Anti-Mouse IgM, u Chain Specific (1:500)	Jackson ImmunoResearch	Cat. # NC0323536
Biotin-SP-AffiniPure Donkey Anti-Mouse IgG (H+L) (1:500)	Jackson ImmunoResearch	Cat. # NC0141064
Biotin-SP-AffiniPure Donkey Anti-Rabbit IgG (H+L) (1:500)	Jackson ImmunoResearch	Cat. # NC9745676
Biotin-SP-AffiniPure Donkey Anti-Chicken IgY (IgG) (H+L) (1:500)	Jackson ImmunoResearch	Cat. # NC9969673
Biotin-SP-AffiniPure Donkey Anti-Guinea Pig IgG (H+L) (1:500)	Jackson ImmunoResearch	Cat. # NC9121043
Bobcat urine	Maine Outdoor Solutions	Cat. # 91412
5-Bromo-2'-deoxyuridine (BrdU)	Thermo Scientific	Cat. # H27260-06
Calcium Chloride ($CaCl_2$) dihydrate	Acros Organics	Cat. # 423525000
D-Glucose	Sigma	Cat: # G8270
DAPI (1:5000)	Fisher	Cat. # ICN15757401
Dibenzyl ether (DBE)	Sigma	Cat. # 108014
Dimethyl sulfoxide (DMSO)	Fisher	Cat. # BP231-100
EGTA	Sigma	Cat. # E3889
EZ-link Biocytin	ThermoFisher	Cat. # 28022
Fetal bovine serum (FBS)	Fisher (Gibco)	Cat. # 26140079
Foraging mix	VWR	Cat. # 89067-313
Flowmi 40 μm cell strainers	Sigma	Cat. # BAH136800040-50EA
Fluoromount-G	SouthernBiotech	Cat. # OB100-01
GlutaMAX Supplement	Fisher (Gibco)	Cat. # 35050061
Guanosine 5'-triphosphate (GTP) sodium salt	Sigma	Cat. # 51120
Hanks Buffered saline solution (HBSS)	Gibco	Cat. # 14175079
HEPES	Sigma	Cat. # H3375
Hydrogen peroxide 30%	DSS Stockroom	Cat. # H323500
Low melting point agar	Fisher	Cat. # 16-520-050
LS columns	Miltenyi Biotec	Cat. # 130-042-401
Magnesium Chloride ($MgCl_2$) hexahydrate	Sigma	Cat. # M9272
Magnesium Sulfate ($MgSO_4$) hepta-hydrate	Sigma	Cat. # 230391
Millicell-CM	Millipore	Cat. # PICM03050
Mineral Oil	Sigma-Aldrich	Cat. # 69794
Myelin Removal Beads	Miltenyi Biotec	Cat. # 130-096-733
N-2 supplement (100X)	Fisher (Gibco)	Cat. # 17502048
Papain Dissociation System	Worthington	Cat. # LK003150
Paraformaldehyde (PFA)	Fisher	Cat. # AC416780010

(*Continued on next page*)

Please cite this article in press as: Alderman et al., Delayed maturation and migration of excitatory neurons in the juvenile mouse paralaminar amygdala, Neuron (2023), https://doi.org/10.1016/j.neuron.2023.11.010

Continued

REAGENT or RESOURCE	SOURCE	IDENTIFIER
Penicillin-streptomycin-glutamine (100X)	Fisher (Gibco)	Cat. # 10378016
Potassium Chloride (KCl)	Sigma	Cat. # P4504
Potassium (K) Gluconate	Sigma	Cat. # G4500
QuadroMACS Separator	Miltenyi Biotec	Cat. # 130-090-976
Rnasezap	Fisher	Cat. # AM9780
Streptavidin-horseradish peroxidase (HRP)	Akoya	Cat. # TS-000302
Sodium Bicarbonate ($NaHCO_3$)	Sigma	Cat. # S5761
Sodium Chloride (NaCl)	Sigma	Cat. # S9888
Sodium Citrate Dihydrate	Fisher	Cat. # BP327-500
Sodium Phosphate (NaH_2PO_4) monobasic monohydrate	Sigma	Cat. # S3522
Streptavidin-Cy5	Vector Labs	Cat. # SA-1500; lot # ZH0819
Streptavidin-HRP	Akoya Biosciences	Cat. # TS-000300
Sucrose	Sigma	Cat. # S0389
Sunflower oil	Sigma Aldrich	Cat. # S5007
Tamoxifen	Sigma Aldrich	Cat. # T5648
Tyramide signal amplification (TSA) Cy3 (1:100)	PerkinElmer	Cat. # FP1170; lot # 2525644
Tyramide signal amplification (TSA) Cy5 (1:100)	PerkinElmer	Cat. # FP1117; lot # 2066310
Tyramide signal amplification (TSA) Plus Fluorescein	Akoya Biosciences	Cat. # NEL741001KT
35mm glass bottom petri dish 20mm coverslip	MatTek	Cat. # NC9732969
1x Plus Amplification Diluent	Akoya	Cat. # FP1135
Deposited data		
Single cell sequencing	This paper	NeMO : dat-j84k9fw
Code for analyzing single cell sequencing data	This paper	Github: https://github.com/Sorrells-Lab/Neuron2023scRNA-seq; Zenodo: https://doi.org/10.5281/zenodo.10038618
Experimental models: Organisms/strains		
Mouse: C57BL/6J-Tg(Dcx-mRFP)15Qlu/J	The Jackson Laboratory	Jax: 024905; RRID:IMSR_JAX:024905
Mouse: Dcx-CreERTM::Rosa-LSL -tdTomato	Available upon request from lead contact	N/A
Mouse: C57BL/6Jwild type	The Jackson Laboratory	Jax: 000664; RRID:IMSR_JAX:000664
Mouse: Tshz1-GFP	Available upon request from Kenneth Campbell	N/A
Mouse: Emx1-Cre	The Jackson Laboratory	Jax: 005628; RRID:IMSR_JAX:005628
Mouse: Gsx2-iCre	The Jackson Laboratory	Jax: 025806; RRID:IMSR_JAX:025806
Mouse: Rosa26YFP	The Jackson Laboratory	Jax: 006148 RRID:IMSR_JAX:006148
Oligonucleotides		
Cre: 5′-CTG CCA CCA GCC AGC TAT CAA CTC-3′	IDT	N/A
ER: 5′-CTC AGC ATC CAA CAA GGC ACT GAC-3′	IDT	N/A
Other		
Thermo Sorvall Legend RT Centrifuge	ThermoFisher	Cat. # 75004377
Cryostar NX50	ThermoFisher	Cat. # 14-071-454
DM4 microscope	Leica	N/A

(*Continued on next page*)

Please cite this article in press as: Alderman et al., Delayed maturation and migration of excitatory neurons in the juvenile mouse paralaminar amygdala, Neuron (2023), https://doi.org/10.1016/j.neuron.2023.11.010

Continued

REAGENT or RESOURCE	SOURCE	IDENTIFIER
Nikon Ti2 microscope	Nikon	N/A
TCS SP8 confocal microscope	Leica	N/A
Eppendorf ThermoMixer C	Eppendorf	Cat. # 5382000023
VT1200S vibratome	Leica	N/A
FEI Tecnai G2 Spirit transmission electron microscope	FEI	N/A
Ultramicroscope II	Miltenyi Biotec	N/A

RESOURCE AVAILABILITY

Lead contact

Requests for further information about resources and reagents should be directed to the lead contact Shawn Sorrells (shawn.sorrells@pitt.edu).

Materials availability

The reagents in this study are available from the lead contact upon request.

Data and code availability

- Single cell RNA-seq data have been deposited at NeMO and are publicly available as of the date of publication. NeMO: dat-j84k9fw. Landing page: https://assets.nemoarchive.org/dat-j84k9fw.
- All original code used for single cell RNA-seq analysis is available at Zenodo: (https://doi.org/10.5281/zenodo.10038618) and on the lab's GitHub: (https://github.com/Sorrells-Lab/Neuron2023scRNA-seq).
- Any additional information that would be required to reanalyze the data reported in this work is available from the lead contact upon request.

EXPERIMENTAL MODEL AND STUDY PARTICIPANT DETAILS

Mice

Male and female C57Bl/6J (Jackson labs, Strain #: 000664) wildtype mice used in this study were socially housed (up to 4 mice/cage) on a 12 hour day/night cycle with ad libitum food and water in a pathogen-free facility. All experiments were conducted in accordance with approved protocols by the University of Pittsburgh Institutional Animal Care and Use Committee (IACUC) and following NIH guidelines for animal research. All mice used in this study were healthy and were only used in the manner described for each experiment and did not undergo previous experimental procedures. To create the Dcx-CreER™ mouse line, a transgenic construct using doublecortin (Dcx) BAC clone (GENSAT1-BX214) to express CreER™ recombinase[108] was injected into fertilized C57Bl/6J eggs. Founder line was established by expression testing via subsequent crosses to a Rosa-LSL-tdTomato reporter.[109] Allele specific genotyping of transgenic mice was performed by PCR with primers (Cre: 5′-CTG CCA CCA GCC AGC TAT CAA CTC-3′) and (ER: 5′-CTC AGC ATC CAA CAA GGC ACT GAC-3′). Only Dcx-CreER females carried the transgene so all experiments using these mice used females. Tshz1-GFP mice were a gift from Kenneth Campbell (Cincinnati Children's Hospital) and Dcx-mRFP (monomeric red fluorescent protein) mice were a gift from Qiang Lu (City of Hope). Male and female *Emx1-*^{Cre} mice (Jackson labs *Emx1ires cre*. Strain #: 005628) and *Gsx2-*^{iCre} mice (Jackson labs *Gsh2-*^{iCrepA}. Strain #: 025806) were both crossed to Rosa26EYFP+/+mice (Jackson labs *R26R-EYFP*. Strain #: 006148).

Human postmortem tissue

Twenty-one post-mortem specimens were examined for this study (Table S7). Tissue was collected with previous patient or next-of-kin consent in strict observance of the legal and institutional ethical regulations in accordance with each participating institution: 1. In accordance with institutional guidelines and study design approval by the Committee for Oversight of Research and Clinical Training Involving Decedents (CORID) at the University of Pittsburgh. 2. Specimens collected at the University of Pittsburgh Medical Center (UPMC) had IRB approved research informed consents along with HIPAA authorizations signed by parents or responsible guardians. 3. The University of California, San Francisco (UCSF) Committee on Human Research. Protocols were approved by the Human Gamete, Embryo and Stem Cell Research Committee (Institutional Review Board) at UCSF. We collected tissue blocks from the temporal lobe, rostrally from the amygdaloid complex to the caudal end of the inferior horn of the lateral ventricle. Samples were either flash frozen or fixed in 4% paraformaldehyde (PFA) or 10% formalin for >24h. Brains were cut into ~1.5 cm blocks, cryoprotected in a series of 10%, 20%, and 30% sucrose solutions, and then frozen in an embedding medium, OCT. Blocks of the medial temporal lobe

were cut into 20 micron sections on a cryostat (Leica CM3050S, or Thermo Scientific NX50) and mounted on glass slides for immunohistochemistry.

METHOD DETAILS

5-bromo-2-deoxyuridine (BrdU) administration

To generate timed pregnant mice, C57Bl/6J females were paired with a male for 24 hrs and then separated. Pregnant mice were given i.p. injections of 50 mg/kg BrdU (Thermo Scientific, catalog # H27260-06) dissolved in sterile saline at specific embryonic time points, considering the day post pairing as E0.5. For postnatal BrdU experiments, C57Bl/6J mice were given i.p. injections of 50 mg/kg BrdU singly or once-daily for seven days (n= 5 per time point).

Tamoxifen (TMX) administration

Cre positive Dcx-CreER™::Rosa-LSL-tdTomato mice were given intraperitoneal injections of 10 mg/kg tamoxifen (TMX) (Sigma Aldrich, catalog # T5648) dissolved in sunflower oil (Sigma Aldrich, catalog # S5007) once daily for three days starting at either P21 or P28. Mice were then collected either 2, 5, or 12 days after the final injection (n=4-6 per time point, 5 sections per mouse).

Mouse tissue immunostaining

Mice were anesthetized using an overdose of isoflurane and were transcardially perfused with 1x phosphate buffered saline (PBS) followed by 4% paraformaldehyde (PFA). Brains were postfixed in 4% PFA overnight and sunk in 30% sucrose in 1X PBS solution for 24 hr prior to sectioning on a freezing-sliding microtome at 50 μm. Sections were stored in 1X PBS + 0.05% sodium azide until staining. Unless otherwise indicated, stains were performed on a series of 1 in every 4 sections (200 μm apart). For most staining, a standard protocol was performed: sections were washed in 1x PBS + 0.2% triton (PBST) for 10 min, treated with 0.5% sodium borohydride for 15 min, washed 5 times for 10 min per wash with 1x PBS followed by 1.5 hr incubation in 10% normal donkey serum (NDS) in PBST (block solution). Sections were washed 3 times for 10 min in PBST followed by incubation in primary antibody in block solution overnight (16-24 hrs) at 4 °C. Sections were then washed with PBST 5 times for 10 min per wash before being incubated in secondary antibodies and DAPI (4′,6-diamidino-2-phenylindole) (1:5000 dilution, Fisher, catalog # ICN15757401) in block solution for 90 min at room temperature. The sections were then washed a final time with PBST 5 times for 10 min per wash and then mounted with Fluoromount-G (SouthernBiotech, catalog # OB100-01).

For BrdU co-staining in postnatal brains, sections were washed and then treated with 2N HCl for 30 min at 37 °C, then washed 5 times for 10 min per wash with 1X PBST. Sections were then stained with BrdU primary antibody and other co-stains according to the standard staining protocol above. For BrdU co-staining in embryonic brains, 20 μm cryostat sections were collected using a Cryostar NX50 (ThermoFisher) and mounted on Superfrost Plus slides (Fisher, catalog # 12-544-2) and stored at -80 °C until use. BrdU co-staining in embryonic tissue was performed by first staining for all other primary antibodies according to the standard staining protocol detailed above. The tissue was then treated with 4% PFA for 10 min at room temperature, followed by incubation in 2N HCl for 20 min at 37 °C, washed 5 times with 10 min per wash, and then stained with BrdU primary antibodies overnight followed by detection using the standard protocol above.

Anatomical boundaries of the developing and adult mouse paralaminar nucleus

The PL nucleus is longest along its rostral-caudal axis (~2.5 mm), and thin along its dorsal-ventral and medial-lateral axes (50-200 μm and 20-90 μm, respectively). Using a nuclear stain like DAPI, in the coronal plane, the PL is visible as a small dense nucleus near the ventral tip of the external capsule on the lateral side of the BLA as a small dense nucleus. Due to its small dimensions in the coronal plane, the PL is difficult to identify without other markers of the region like Dcx or Tbr1. In sagittal sections, at its lateral boundary the PL is ventral to the BLA as a sparse field of cells with small nuclei. In more medial sagittal sections, the region is present rostral to the BLA as a horn-shaped nucleus packed with cells at a high density similar to the adjacent ITCs. In the most medial sagittal sections, the location of the PL is shifted dorsally and rostrally away from the BLA.

In mouse brain atlases, the PL is varyingly indicated as belonging to one or multiple neighboring structures depending on the section level and atlas. In the 2011 Allen sagittal adult mouse brain atlas (Allen Mouse Brain Atlas, mouse.brain-map.org and atlas.brain-map.org), the PL can be seen using the Nissl staining beginning in sagittal section three (in an unlabeled region between the BLA and the endopiriform nucleus) and ending in sagittal section eight (where it is included in the ventral part of the fundus of the striatum). In between these levels it is sometimes identified within the boundaries of the vEN and ITCs. In the Paxinos and Franklin Mouse Brain in Stereotaxic Coordinates (MBSC) sagittal mouse brain atlas (second edition, 2001), lateral edges of the PL are included in the boundaries of the ventral endopiriform, while more medial sections include the PL in the dorsal endopiriform.

Unbiased stereology

Stereological quantifications in the PL and vEN were performed with the optical fractionator probe using Steroinvestigator (MBF Biosciences) on a Leica DM4 microscope. Using a 10x/0.45 NA objective, the boundaries of the PL and vEN were delineated based on the cytoarchitecture visible from DAPI and NeuN staining, which remain constant across the ages examined (e.g., Figures 6F, 6I, 6L, and S3B). $DAPI^+$, Dcx^+ and $NeuN^+$ cells were counted using a 63x/1.40 NA oil-immersion objective. Section thickness was measured

Please cite this article in press as: Alderman et al., Delayed maturation and migration of excitatory neurons in the juvenile mouse paralaminar amygdala, Neuron (2023), https://doi.org/10.1016/j.neuron.2023.11.010

at every counting site. Five mice per age were counted at P7, P14, P21, P35, and P60. Sexes were evenly represented across groups. Five 50 μm sections, each spaced by 200 μm, were counted, which covered the extent of PL and vEN. To minimize section edge damage, a new disposable cutting blade was used for each brain during sectioning on a frozen sliding microtome. Mice in which a section was missing or an ROI was damaged were excluded from counts. To ensure a minimum of 150 objects were counted for each probe run across different sizes of objects and ages, the frame and grid sizes for each probe type were optimized (see Table S5 for a complete list of sampling parameters). For ages P21–P60, all probes were counted with a dissector height of 15μm with 5μm guard zones. Tissue from mice at younger ages, P7 and P14, exhibited greater z-collapse, so we used a dissector height of 13 μm and 3 μm guard zones. The unique point on each counted object (its leading edge) that was used for inclusion/exclusion criteria was the boundary of the soma. Objects were counted if they intersected with a inclusion line of the counting frame or were within the counting frame entirely. The end of the soma and beginning of a process (which was not used for counting) was defined by the inflection point at which the process began to taper away from the soma. All probe runs included in the study had a Gunderson coefficient of error (CE) (Gundersen, 1999) below 0.1. The average Gunderson CEs for each probe and region were: PL DAPI = 0.0757, PL NeuN CE = 0.0590, PL Dcx CE = 0.0667, vEN DAPI CE = 0.0670, vEN NeuN CE = 0.0623, and vEN Dcx CE = 0.0783.

Marker co-expression quantification

For all mouse marker co-expression quantifications, three (for c-Fos, Ki-67, Prox1, Tbr2, pH3, pi5 BrdU quantifications) or five (for all other studies) 50 μm sections of tissue evenly spaced by 200 μm (1 out of every 4 sections) were evaluated (n=5 per experiment). For Dcx, NeuN, transcription factor, and lineage co-localization quantifications we used a Leica TCS SP8 confocal microscope or a Nikon Ti2 series confocal microscope (20x/0.75 NA objective, 10x/0.4 for c-Fos co-expression study only) to collect system optimized z-stacks of the entire tissue z-height of the PL. Co-expression of the specified transcription marker and Dcx^+NeuN^+ and Dcx^-NeuN^+ cells in the PL was quantified using ImageJ (Rasband, W.S., ImageJ, U. S. National Institutes of Health, Bethesda, Maryland, USA, https://imagej.nih.gov/ij/, 1997-2018). Individual channels were merged and assessed across each frame of the z-stack. For Dcx-CreER™::Rosa-LSL-tdTomato quantifications, only mice with >2 tdT^+ cells in the PL (across 5 sections) were analyzed. We used a Leica TCS SP8 confocal microscope (10x/0.40 NA objective) to collect system optimized z-stacks of the entire tissue z-height of the PL and quantified co-expression using ImageJ. For BrdU quantifications, we used StereoInvestigator (MBF Biosciences) connected to a Leica DM4 microscope. Boundaries of the PL and vEN were traced using a 10x/0.45 NA objective and co-localization was assessed across the z-height of the section with a 63x/1.40 NA oil-immersion objective. Dcx^+ cells were classified as either round or elongated, as described below.

Cell morphology reconstructions and mapping

To map the location of Dcx^+ neurons with round or elongated morphology, cells were counted and traced using Neurolucida (MBF Biosciences) on a Leica DM4 microscope with a 10x/0.45 NA objective (for ROI delineation) and a 63x/1.40 NA oil-immersion objective (for cell counting and cell tracing) (n=6, 3 sections per animal). Within a 1.5 mm square region centered on the PL, we traced the outline of the BLA, ITCs, vEN, layer 2 of the piriform cortex, and PL across 3 evenly-spaced sagittal sections. The location of every Dcx^+ cell within that square was mapped together with information about co-expression and morphology of each cell. For both human and mouse quantifications, a Dcx^+ cell was classified as elongated if its soma was fusiform and it also had one simple (unbranched) linear projection. A Dcx^+ cell was classified as round if its soma was spherical and/or if it had more than one process and/or if it had a single process with multiple branches.

Olfactory stimulus exposure

For the predator odor experiment, juvenile (P25-27; n=10) and adult (P73-P85; n=14) male and female mice were single housed for three to seven days prior to testing. Each day during this period, mice were habituated to the procedure room. On the final day, mice were taken to the procedure room and exposed to either 400 μl of mineral oil or predator urine (bobcat urine, Maine Outdoor Solutions) on a cotton ball stuffed down into a 15 ml falcon tube for 30 minutes followed by immediate transcardial perfusion. For the novel odorant experiment, juvenile (P25-P27) and adult (P60-P100) male and female mice were single housed for four to seven days prior to testing. Home cage animals were collected directly from the home cage followed by immediate transcardial perfusion (n=13). For each condition mice were exposed to the tube with odorant in the home cage on the rack for 30 minutes and then collected immediately (n=5-7 per group). On the day of collection, 400 μl of mineral oil (Sigma-Aldrich), or 400 μl of novel odorant diluted 1:100 in mineral oil (acetophenone, Sigma-Aldrich) was added to a cotton ball stuffed down into a 15 ml falcon tube so that the mice could not reach the cotton ball. Novel food odorant tubes were prepared by filling 15 ml falcon tubes to the 5 ml line with novel food (foraging mix, VWR) and sealed with a cotton ball so the mice could not access the food. New gloves and transfer containers were used for each animal to minimize exposure to other olfactory stimuli. No mice were excluded from this experiment.

Transmission electron microscopy and immunogold labeling

Mice (P14, P21 and P28; n=6 per age, embedding 3 sections / animal) were deeply anesthetized and perfused with 0.9% saline followed by 2% paraformaldehyde (PFA) and 2.5% glutaraldehyde (EMS) in 0.1 M phosphate buffer (PB). Brains were dissected and post-fixed overnight at 4 °C in the same fixative solution and subsequently, 200 μm sagittal sections were prepared using a Leica

VT1200S vibratome (Leica Microsystems). Slices were further post-fixed in 2% osmium tetroxide in 0.1 M PB for 1.5 hours at room temperature, washed in deionized water, and partially dehydrated in 70% ethanol. Samples were then incubated in 2% uranyl acetate in 70% ethanol in the dark for 2.5 h at 4 °C. Brain slices were further dehydrated in ethanol followed by propylene oxide and infiltrated overnight in Durcupan ACM epoxy resin (Fluka, Sigma-Aldrich). The following day, the samples were transferred to fresh resin and were cured for 72 h at 70 °C. Following resin hardening, semithin sections (1.5 μm) were obtained with a diamond knife using a Ultracut UC7 ultramicrotome (Leica). Sections were mounted onto glass microscope slides and lightly stained with 1% toluidine blue. After identification of the PL by light microscopy, selected semithin sections were glued with Super Glue-3, Loctite (Henkel) to resin blocks and subsequently detached from the glass-slides by repeated freezing (in liquid nitrogen) and thawing. Ultra-thin sections (60–80 nm) were obtained with the ultramicrotome from detached semi-thin sections, and further stained with lead citrate (Reynolds' solution). The samples were examined with a FEI Tecnai G^2 Spirit transmission electron microscope at 80 kV (FEI Europe) equipped with a XAROSA CMOS digital camera (EMSIS GmbH).

For pre-embedding immunogold stains (P21; n=4 per age, embedding 3 sections / animal), samples were fixed with 4% PFA in 0.1 M PB and cut into 50 μm sagittal sections using a vibratome. Pre-embedding immunogold stainings were performed as previously described.[110] Sections were contrasted with 1% osmium tetroxide, 7% glucose in 0.1 M PB and embedded in Durcupan epoxy resin. Subsequently, 100-150 serial semithin sections (1.5 μm) were obtained with the ultramicrotome, mounted onto glass-slides, and stained with 1% toluidine blue. Selected semi-thin sections were processed as described above to obtain ultrathin sections prior to examination by TEM.

Electrophysiology

C57Bl/6J mice (P21-P28; n=10) were anesthetized with isofluorane and decapitated. Brains were dissected and placed into ice-cold cutting ACSF, containing: Sucrose 234 mM, D-Glucose 11 mM, KCl 2.5 mM, $NaHCO_3$ 26 mM, NaH_2PO_4 1.25 mM, $MgSO_4$ 7 mM, $CaCl_2$ 0.5 mM. Sagittal sections (275 μm thick) were sliced using a Leica V1200 vibratome. Sections containing the PL were transferred to recording ACSF, containing: NaCl 125 mM, KCl 3.5 mM, $CaCl_2$ 2 mM, $MgCl_2$ 1 mM, NaH_2PO_4 1.25 mM, $NaHCO_3$ 26 mM, D-Glucose 10 mM. This solution was initially held at 34 °C for 30 minutes to facilitate slice recovery, before cooling to room temperature for the duration of the experiment. All solutions were adjusted to 7.4 pH and 300 mOsm and were bubbled with carbogen (95% CO_2/5% O2) during all steps. All chemicals were supplied by Sigma (St Louis Mo). Patch pipettes (5-9 MΩ) were pulled from borosilicate glass pipettes (Sutter Instruments) using a vertical 2-stage puller (Narishige PP-830) and filled with an internal solution containing: K-gluconate 145 mM, HEPES 10 mM, EGTA 1 mM, Mg-ATP 2 mM, Na_2-GTP 0.3 mM, $MgCl_2$ 2 mM, and biocytin 0.5% (ThermoFisher). This solution was adjusted to 7.3 pH and 290-300 mOsm, and 0.5% biocytin was added on the day of the experiment.

Patch-clamp electrophysiology was conducted using a Nikon upright microscope and a 60X water immersion objective, and slices were held in a chamber containing recording ACSF with a flow rate of 2-3 mL/min at room temperature. The PL was identified by its anatomical position between ventral endopiriform, striatum and basolateral amygdala and its higher cell density than nearby regions. Whole-cell patch-clamp recordings (n = 25 cells from 10 mice) were obtained using a MultiClamp 700A amplifier, Digidata 1550B digitizer, and pClamp 10 software (Axon Instruments, Molecular Devices). Electrical signals were sampled at 20Hz. During whole-cell current clamp recordings, cells with access resistances greater than 30 MΩ or resting membrane potential drift >5 mV were discarded. 1-second long hyperpolarizing and depolarizing current steps were applied, in increasing intervals of 5 pA, up to ±100 pA. Next, voltage clamp recordings were obtained to record sEPSCs (inward currents at -70mV holding) and sIPSCs (outward currents at -40mV holding potential).

Analysis was performed in Clampfit 10. Input resistance was calculated from the linear slope of the voltage responses to the first 3-4 hyperpolarizing current steps. Time constant was calculated from an exponential curve to a 10 pA hyperpolarizing current. Action potential properties were analyzed from the first elicited action potential (at the rheobase current). Threshold was measured as the first point with dV/dt > 20 mV/msec. Amplitude was calculated as the difference between peak voltage and threshold. Spike duration was measured as the width of the spike halfway between threshold and peak. Depolarization/repolarization ratio was calculated from the largest value depolarization and repolarization slopes.

Following recordings, sections (n=25 cells from n=10 mice; n=18 biocytin filled neurons) were fixed in 4% PFA overnight at 4 °C, and then washed in PBST. To label biocytin-filled cells, sections were incubated for 2 hours at RT in block solution. Then, primary antibody (Rb anti-Dcx) and Streptavidin-Cy5 were added to fresh block solution, and sections were incubated overnight at 4 °C. Sections were then washed with PBST, 3 times for 10 minutes per wash, and 2 times for 30 minutes per wash. Then, sections were incubated in secondary antibodies and streptavidin dye conjugate in block solution, overnight at 4 °C. Following secondary incubation, sections were again washed with PBST, 3 times for 10 minutes per wash, and 2 times for 30 minutes per wash. Finally, sections were mounted to slides, allowed to dry completely, and coverslipped with Fluoromount-G with DAPI (SouthernBiotech).

iDISCO staining and light sheet microscopy

For whole mount imaging, the iDisco tissue clearing method was used.[56] Wildtype C57Bl/6 mice (n=8–10 at P7 and P21) were perfused with 4% paraformaldehyde, fixed overnight at 4 °C, and then washed in PBS. Prior to immunostaining, tissue was dehydrated using increasing concentrations of methanol in distilled water (20%, 40%, 60%, 80%, 100%, 100%, 1 hour each at RT), bleached overnight in 5% H_2O_2 in 100% methanol at 4 °C, and then gradually rehydrated (80%, 60%, 40%, 20% methanol, then

PBS with 0.2% Triton, 1 hour each at RT). Bleached samples were incubated in permeabilization solution (PBS with 0.2% Triton, 20% DMSO, 0.3M glycine) and then in blocking solution (PBS with 0.2% Triton, 10% DMSO, 6% Normal Donkey Serum), each for 2 days at 37 °C. Primary antibody incubation was performed in PTwH (PBS with 0.2% Tween-20 and 10 μg/ml heparin) + 5% DMSO and 3% Normal Donkey Serum, 4 days at 37 °C. Samples were washed in PTwH over 24 hours at RT (5-6 washes of increasing duration), before incubation in secondary antibody in PTwH + 3% Normal Donkey Serum, 4 days at 37 °C. Another series of 5-6 washes in PTwH over 24 hours at RT were performed before proceeding to clearing steps.

Clearing was performed by dehydrating samples in increasing concentrations of methanol in distilled water (20%, 40%, 60%, 80%, 100%, 1 hour each at RT), then incubating in a solution of 66% dichloromethane (DCM, Sigma 270997) in methanol for 3 hours at RT. 2 washes of 100% DCM (15 minutes each at RT) were performed before placing samples in dibenzyl ether (DBE, Sigma 108014) for clearing and imaging. Samples were imaged in DBE via light sheet microscopy (Ultramicroscope II, Miltenyi Biotec) equipped with an sCMOS camera (Andor NEO 5.5) and a 2x Olympus objective lens. Cleared samples were stored long-term in DBE in glass containers in the dark. Light sheet datasets were imported into Imaris 9.1 (Bitplane) for 3D visualization. No masking was performed. Following automatic rendering using the 'MIP' setting, movies of 3-D datasets were generated using the 'animation' tool.

Time-lapse microscopy and migratory neuron tracking

For time-lapse microscopy, P0.5-P3 Dcx-mRFP (n=4) mice were anesthetized in wet ice before being sprayed with 70% ethanol and decapitated with sterilized scissors. The brain was then extracted and placed in chilled ACSF (glucose 25 mM, NaCl 125, KCl 2.5 mM, $MgCl_2$ 1 mM, $CaCl_2$ 2 mM, $NaHCO_3$ 2.5 mM, Na_2HPO_4 1.25 mM) or HBSS (Gibco, catalog # 14175079) that had been bubbled with carbogen (95% O_2 and 5% CO_2) for 30 minutes while on wet ice. Brains were embedded in blocks with 3.5% low melting point agar (Fisher, catalog # 16-520-050) heated to 37 °C. After the agar had solidified, 350 μm sagittal sections were prepared using a vibratome (Leica VT 1200S) with carbogen-bubbled ACSF or HBSS in the sectioning chamber that was externally packed with wet ice. Sections were transferred onto sterile membrane culture inserts (Millicell-CM, Millipore; 0.4 μm pore size, 30 mm diameter, catalog# PICM03050). These were placed into either a glass-bottom coverslip petri dish (MatTek, catalog # NC9732969) or a six-well plate containing pre-incubated slice culture medium (1.5-2 mL per well) that consisted of 66.6% Basal Medium Eagle (BME) with phenol red (Thermofisher, catalog# 21010046), 25% HBSS, 5% fetal bovine serum (FBS) non-heat inactivated (Gibco, catalog # 26140079), 1.3% of 33% glucose, 1% penicillin-streptomycin-glutamine (P/S/L-glut) (Gibco, catalog # 10378016), 1% GlutaMAX (L-glut 200 mM) (Gibco, catalog# 35050061), and 1% N-2 (Fisher (Gibco), catalog # 17502048). Cultures were imaged on the microscope in a humidified incubator (okoLab Transparent Cage Incubator DMi8, catalog # 158206046) with a heated and humidified gas mixture (5% O_2, 5% CO_2, at 37 °C). Imaging was every 20-30 min using a Leica Sp8 confocal resonance scanner and a 10x/0.40 NA objective with 2-3x digital zoom. A minimum of 3 technical replicates were conducted for quantifications. Traces of migrating neurons were generated using the ImageJ manual tracking feature. The coordinates of the soma of each migrating neuron was recorded for each time frame it was visible within the optical section. Those coordinates were then used to calculate each neuron's total distance traveled and total displacement, the time interval over which the cell was moving was then used to calculate migration speed.

Human tissue immunofluorescence

Frozen slides were allowed to equilibrate to room temperature for 3 hours and rehydrated in PBS prior to antigen retrieval at 95°C in 10 mM sodium citrate buffer, pH=6.0. Slides were washed with TNT buffer (0.05% TX100 in PBS) for 10 minutes, placed in 1% H2O2 in PBS for 45 minutes and then blocked with TNB solution (0.1 M Tris-HCl, pH 7.5, 0.15 M NaCl, 0.5% blocking reagent from Akoya Biosciences, catalog # NEL741001KT) for 1 hour. Slides were incubated in primary antibodies overnight at 4 °C and in biotinylated secondary antibodies (Jackson Immunoresearch Laboratories) for 2.5 hours at room temperature. All antibodies were diluted in TNB solution. For most antibodies, the conditions of use were validated by the manufacturer (antibody product sheets). When this information was not provided, we performed control experiments, including no primary antibody (negative) controls and comparison to mouse staining patterns. Sections were then incubated for 30 min in streptavidin-horseradish peroxidase that was diluted (1:200) with TNB. Tyramide signal amplification (PerkinElmer) was used for some antigens. Sections were incubated in tyramide-conjugated fluorophores for 5 minutes at the following dilutions: Fluorescein: 1:100; Cy3: 1:100; Cy5: 1:100. After several PBS rinses, sections were mounted in Fluoromount-G (Southern biotech, catalog # OB100-01) and coverslipped. Staining was conducted in technical triplicates prior to analysis.

Single cell dissociation and RNA-sequencing

Four juvenile (P22) C57Bl/6J littermates (two male and two female) were deeply anesthetized using an overdose of isoflurane followed by decapitation. Brains were extracted and then embedded in blocks with 3.5% low melting temp agar (Fisher, catalog # 16-520-050) heated to 37 °C in a waterbath. After the agar had solidified, 350 μm sagittal sections were prepared using a vibratome (Leica, VT1200S) with chilled carbogen-bubbled HBSS in the sectioning chamber that was externally packed with wet ice. Sections were collected using a cut sterile disposable pipette (VWR catalog # 76285-362) and then placed in L-15 media on ice. The PL and vEN from 5-6 sections per brain were hand dissected using a sterile pulled glass pipette under a dissecting microscope. The tissue was transferred to Papain-EBSS (Worthington, catalog # LK003150). Tissue was digested for 30 mins at 37°C in a thermomixer at 900 RPM. The tissue was then mechanically dissociated using a sterile RNAse-free wide bore P1000 pipette tip for 20 s, and then with a sterile fire-polished pasteur pipette for 5 min. Tissue was digested for 10 min at 37°C, and dissociated with the pasteur pipette for

Please cite this article in press as: Alderman et al., Delayed maturation and migration of excitatory neurons in the juvenile mouse paralaminar amygdala, Neuron (2023), https://doi.org/10.1016/j.neuron.2023.11.010

another 2 min. Cells were centrifuged for 5 min, 300 RCF at 4°C, and the pellet was resuspended with DNAase/ovomucoid inhibitor according to manufacturer's protocol (Worthington). Cells were incubated in Red blood cell lysis buffer (BioLegend, catalog # 420301) for 3 min on wet ice. Samples were then filtered with a FlowMi 40 μm cell strainer (Sigma, catalog # BAH136800040-50EA) followed by a filter wash using 500uL 1% BSA-PBS. To remove myelin, the cell suspension was incubated with Myelin Removal Beads (Miltenyi Biotec, catalog # 130-096-733) (6 μl/brain) for 15 min on wet ice. Cells were washed with 0.5% BSA-PBS and transferred to MACS LS columns (Miltenyi Biotec, catalog # 130-042-401) and QuadroMACS Separator (Miltenyi Biotec, catalog # 130-090-976). The effluent was collected and loaded into two wells of a 10x Genomics Chromium X series controller. Libraries were sequenced in a Novaseq 6000 system (Illumina).

Single cell RNA sequencing analysis

Sequencing reads were aligned using CellRanger v7.1.0 via the 10x Genomics Cloud Analysis system, with the Single Cell 3' Gene Expression reference library. Quality control and pre-processing steps consisted of discarding low-quality cells by removing barcodes with low numbers of genes (nFeature_RNA < 2,000; nCount_RNA < 4,000), and likely doublets based on high numbers of molecules detected per cell (nCount_RNA > 30,000), or cells clustered with them. We also excluded barcodes with more than 10% of reads belonging to mitochondrial genes. We used SCTransform as a normalization method and 30 dimensions for Uniform Manifold Approximation and Projection (UMAP) dimension reduction function in Seurat v.4.2.[111] Principal component (PC) analysis was performed on the normalized data and 10 dimensions (mouse dataset) or 15 dimensions (human dataset) were used for UMAP dimension reduction. Dot plots and feature plots were prepared using Seurat v4.2. To identify differentially expressed genes between clusters we used a Wilcoxon rank sum test in Seurat v4.2 on the non-transformed RNA data and the results of these tests are in Tables S3 and S4.

Open source gene expression analysis

Single-nuclei RNA sequencing of the human amygdala from 4-15 years old[6] was re-analyzed in R version 4.1.2 (R Core Team (2022). R: A Language and Environment for Statistical Computing. R Foundation for Statistical Computing, Vienna, Austria. <https://www.R-project.org/>) using the Seurat package (v5) and Uniformed Manifold Approximation and Projection (UMAP) for dimension reduction with a dimensionality of 30 and resolution set to 1.5. The cluster containing immature PL neurons was identified based on selective expression of positive PL markers. Genes in this cluster with pct.2 $\leq$ 0.2 were examined for expression levels of the corresponding mouse gene in the mouse PL in the Allen Brain Atlas *in situ* hybridization data (Allen Mouse Brain Atlas, mouse.brain-map.org).[112]

Statistical analysis

Statistical significance was defined as * = $p < 0.05$, ** = $p < 0.01$, *** = $p < 0.001$, **** = $p < 0.0001$. For comparison of multiple groups we used one- or two-way analysis of variance (ANOVA) with post-hoc multiple comparison tests (Tukey, Holm-Sidak, or Dunnett's test). When comparing two groups (electrophysiology), we used unpaired t-test with Shapiro-Wilk post-hoc normality test. Most quantifications are shown as mean ± SEM or ± SD (electrophysiology). An alpha of $p < 0.05$ was used for hypothesis testing to represent a statistically significant difference. All statistical tests were conducted with GraphPad Prism (v.9).